Geoscientific
Model Development
Discussions

Optimizing a dynamic fossil fuel CO_2 emission model with CTDAS (v1.0) for an urban area using atmospheric observations of CO_2, CO, NO_x, and SO_2

Ingrid Super[1,2], Hugo A.C. Denier van der Gon[1], Michiel K. van der Molen[2], Stijn N.C. Dellaert[1], Wouter Peters[2,3]

[1]Department of Climate, Air and Sustainability, TNO, P.O. Box 80015, 3508 TA Utrecht, Netherlands

[2]Meteorology and Air Quality Group, Wageningen University, P.O. Box 47, 6700 AA Wageningen, Netherlands

[3]Centre for Isotope Research, Energy and Sustainability Research Institute Groningen, University of Groningen, Nijenborgh 4, 9747 AG Groningen, Netherlands

Correspondence to: Ingrid Super (ingrid.super@tno.nl)

11 **Abstract.** We present a modelling framework for fossil fuel CO_2 emissions in an urban environment, which allows

12 constraints from emission inventories to be combined with atmospheric observations of CO_2 and its co-emitted

13 species CO, NOx, and SO_2. Rather than a static assignment of average emission rates to each unit-area of the urban

14 domain, the fossil fuel emissions we use are dynamic: they vary in time and space in relation to data that describe

15 or approximate the activity within a sector, such as traffic density, power demand, 2m temperature (as proxy for

16 heating demand), and sunlight and wind speed (as proxies for renewable energy supply). Through inverse

17 modelling, we optimize the relationships between these activity data and the resulting emissions of all species

18 within the dynamic fossil fuel emission model, based on atmospheric mole fraction observations. The advantage

19 of this novel approach is that the optimized parameters (emission factors and emission ratios, N=44) in this

20 dynamic model (a) vary much less over space and time, (b) allow a physical interpretation of mean and uncertainty,

21 and (c) have better defined uncertainties and covariance structure. This makes them more suited to extrapolate,

22 optimize, and interpret than the gridded emissions themselves. The merits of this approach are investigated using

23 a pseudo-observation-based ensemble Kalman filter inversion setup for the Dutch Rijnmond area at 1x1 km

24 resolution.

25 We find that the dynamic fossil fuel model approximates the gridded emissions well (annual mean differences <

26 2 %, hourly temporal r2 = 0.21–0.95), while reported errors on the underlying parameters allow a full covariance

27 structure to be created readily. Propagating this error structure into atmospheric mole fractions shows a strong

28 dominance of a few large sectors and a few dominant uncertainties, most notably the emission ratios of the various

29 gases considered. If these are either sufficiently well-known a-priori, or well-constrained from a dense observation

30 network, we find that including observations of co-emitted species improves our ability to estimate emissions per

31 sector relative to using CO_2 mole fractions only. Nevertheless, the total CO_2 emissions can be well-constrained

32 with CO_2 as only tracer in the inversion. Because some sectors are sampled only sparsely over a day, we find that

33 propagating solutions from day-to-day leads to largest uncertainty reduction and smallest CO_2 residuals over the

34 14 consecutive days considered. Although we can technically estimate the temporal distribution of some emission

35 categories like shipping separate from their total magnitude, the controlling parameters are difficult to distinguish.

36 Overall, we conclude that our new system looks promising for application in verification studies, provided that

37 reliable urban atmospheric transport fields and reasonable a-priori emission ratios for CO_2 and its co-emitted

38 species can be produced.

1 Introduction

Within the 2015 Paris Agreement, 195 nations agreed with a climate action plan in which each nation sets its own targets for carbon emission reductions and reports all efforts regularly to the UNFCCC (UNFCCC, 2015). An important role in reaching emission reduction targets is laid out for cities, which emit a large portion of the global fossil fuel CO_2 emissions (about 70 % according to the International Energy Agency (IEA, 2008)). The Paris Agreement also states that parties should strengthen their cooperation, also with respect to the sharing of information and good practices. Within this context it becomes increasingly important to map fossil fuel emissions and to quantify emission trends, both at the country- and city-level.

Most country-level greenhouse gas emission estimates reported to the UNFCCC are currently based on yearly fuel consumption data (bottom-up method), and are often spatiotemporally disaggregated using activity data and proxies to create spatially explicit emission inventories (Kuenen et al., 2014; Hutchins et al., 2017). Although the yearly national estimates are reasonably accurate (estimated uncertainty for developed countries is less than 8 % for CO_2 (Monni et al., 2004; Fauser et al., 2011; Andres et al., 2014)), their uncertainty increases rapidly when disaggregating them towards finer spatiotemporal resolutions (Ciais et al., 2010; Nassar et al., 2013; Andres et al., 2016). A method to improve emission estimates is using transport models in combination with independent observations of atmospheric mole fractions (Palmer et al., 2018), called data assimilation (DA) or inverse modelling (a top-down method). Recently, efforts have been made to apply DA techniques to the urban environment (McKain et al., 2012; Brioude et al., 2013; Lauvaux et al., 2013; Bréon et al., 2015; Boon et al., 2016; Lauvaux et al., 2016; Staufer et al., 2016; Brophy et al., 2018), but several challenges and unexploited opportunities remain.

First, urban DA studies have tried to constrain the total fossil fuel flux to validate bottom-up CO_2 inventories, often without considering the underlying emission process that caused the mismatch between observed and modelled concentrations. As one of very few exceptions, Lauvaux et al. (2013) used the $CO:CO_2$ concentration ratio to conclude that the emission reduction in Davos during the World Economic Forum 2012 was likely related to reduced traffic emissions, but without a quantification. However, emission reduction policies usually target specific source sectors. Therefore, an increase in fossil fuel emissions from one source sector can cause the total CO_2 emissions to appear stable, although a policy targeting another source sector can be effective in itself. To monitor the effect of each measure independently it becomes essential to attribute changes in the total CO_2 emissions to these policies and thus to specific source sectors. It is, therefore, not sufficient to constrain the total CO_2 flux, but we need to differentiate the total CO_2 signal into signals from the different source sectors. One way to accomplish this is by using additional measurements of co-emitted species and isotopes. Such measurements have previously been used in modelling studies to differentiate between biogenic and anthropogenic emissions or between fuel types (Djuricin et al., 2010; LaFranchi et al., 2013; Lopez et al., 2013; Turnbull et al., 2015; Fischer et al., 2017; Super et al., 2017b; Brophy et al., 2018; Graven et al., 2018), but also to separate between different fossil fuel sources (Lindenmaier et al., 2014; Super et al., 2017a; Nathan et al., 2018).

Second, for urban DA the fine scales (less than 1km and less than 1 hour) need to be resolved, therefore putting a higher demand on the atmospheric transport models. For example, Boon et al. (2016) mentioned that sources with a small spatial extent (point sources) are not correctly represented on a 2x2 km^2 grid, while these sources have a significant impact on the locally observed mole fractions. Concurrently, we have previously shown that a plume model improves the representation of sources with a limited spatial extent. Moreover, we found that the description

79   of short-term variations in the wind direction by the Eulerian WRF model in the vicinity of an urban area is poor

80   (Super et al., 2017a).

81   Third, the prior emissions also need to have a higher resolution for urban-scale studies to resolve the dominant

82   spatiotemporal variations. Previous studies have often used high-resolution emission maps developed specifically

83   for that region, using local data as much as possible (Zhou and Gurney, 2011; Bréon et al., 2015; Boon et al., 2016;

84   Lauvaux et al., 2016; Rao et al., 2017; Gurney et al., 2019). Yet such emission maps are only available for a few

85   data-rich regions. For other regions, continental or global emission maps (such as MACC or EDGAR) can be used

86   if downscaling is applied to reach the high resolution required for urban-scale inversions. For example, the

87   temporal downscaling can be done using typical daily, weekly and monthly profiles for each source sector (Denier

88   van der Gon et al., 2011), which are based on activity data (e.g. traffic counts) averaged over several years and/or

89   a large region. Spatial downscaling often involves proxies like population density. This spatiotemporal

90   downscaling introduces a large additional uncertainty due to uncertainties in the proxies. For example, Hogue et

91   al. (2016) have found an uncertainty of 150 % in the 1x1 ° fossil fuel CO_2 emissions for the US, whereas Ciais et

92   al. (2010) estimated the uncertainty of regional European emissions at 100 km resolution to be about 50 %.

93   Quantification of the uncertainty at an even higher resolution for urban applications has so far been limited (Andres

94   et al., 2016) (Super et al., 2019), also for most local inventories, while a correct definition of the prior error

95   covariance matrix for an inversion is important to get reliable output (Chevallier et al., 2006; Boschetti et al.,

96   2018). This currently complicates the application of DA studies to urban areas.

97   Here, we describe the development of an urban-scale DA framework (based on the CarbonTracker Data

98   Assimilation Shell (CTDAS)) which uses a dynamic fossil fuel emission model as a prior and optimizes the

99   parameters of this model. The dynamic fossil fuel emission model uses a wide range of (statistical) data to calculate

100 CO_2 emissions per source sector at high spatiotemporal resolution (1x1 km2 and hourly). The emission model is

101 dynamic in the sense that its formulation allows emissions to change as a function of rapidly varying conditions

102 in the emission landscape, such as the outside temperature, the traffic density, or availability of wind and solar

103 radiation for sustainable power generation. Using such information enables the calculation of dynamic emissions

104 in near real-time, as opposed to the construction of a static emission map based on statistical downscaling.

105 Moreover, the emission model can supply spatiotemporal emission uncertainties and error correlations between

106 source sectors, based on the estimated uncertainty of its model parameters. Since many of these parameters are

107 also used in bottom-up accounting of emissions, their uncertainty is often better established than the uncertainty

108 in the total emissions themselves. Finally, we use the dynamic emission model to calculate emissions of other co-

109 emitted species (CO, NO_x and SO_2) from the CO_2 emissions using source sector specific emission ratios. These

110 co-emitted species are included in the DA system to facilitate source attribution, which is possible due to the

111 distinct emission ratios of different source sectors. The overall aim of this study is to explore how our dynamic

112 fossil fuel emission model and additional tracers can be used to overcome the known limitations in anthropogenic

113 CO_2 inverse modelling described above. The research questions are:

114   1. Can our dynamic fossil fuel emission model represent the spatiotemporal structure of a high-resolution

115   emission inventory, and what does it add to that on small scales?

116   2. Is the addition of co-emitted species beneficial for the attribution of CO_2 signals to specific source sectors,

117   and which observations help most in that effort?

118   3. Does the prior error covariance structure that we build with the dynamic emissions model help the
119   optimization, and what can we learn from the posterior error covariance estimate?

120   In the inverse part of this study we use observing system simulation experiments (OSSEs, experiments using
121   pseudo-observations), applied to the urban-industrial complex of Rotterdam (Netherlands). This choice allows us
122   to test our new approach, while with real observations the errors in non-fossil and background fluxes, model
123   structure, and model transport will likely dominate the results (Tolk et al., 2008; Super et al., 2017a; He et al.,
124   2018) and reduce the ability to evaluate the methodology. First, we give an overview of the dynamic fossil fuel
125   emission model and demonstrate its applicability to the domain, followed by an introduction to the DA system
126   components and the model settings. Then we discuss the different experiments in which we start with the
127   comparison of different network configurations, one with only CO_2 and one including co-emitted species to
128   examine the ability to attribute CO_2 emissions to specific source sectors, and different state vectors. Another
129   experiment is used to examine the importance of propagating posterior parameters values and covariances. Finally,
130   we address the effect of cross-correlations.

131   **2 Methods**

132   **2.1 The dynamic emission model**

133
134   **Figure 1. Map of the domain covered (Randstad area, the Netherlands) within this study, including major cities**
135   **Amsterdam, Rotterdam, The Hague, and Utrecht (underlined). The squares show the locations of the measurement**
136   **sites within the urban network configuration. The area of this domain is approximately 77x88km. Source: © Google Maps.**

137   Although generally applicable, the dynamic emission model is initially developed for the Netherlands and focused
138   on Rotterdam (Fig. 1). This is one of the major cities in the Netherlands (about 625,000 inhabitants) with the
139   largest sea port of Europe to its west. It is located in a larger urbanized area (Randstad, about 7 million inhabitants)
140   with The Hague, Amsterdam and Utrecht being other major cities. A large area to the southwest of The Hague is
141   covered with glasshouses. The Rotterdam area is characterized by a complex mixture of residential and industrial
142   activities and therefore we distinguish five source sectors and a total of ten sub-sectors to construct its emissions
143   (see Table 1). Note that, for simplicity, only the largest source sectors are included, which are responsible for >95

5

144 % of the CO_2 emissions in the area. The main goal is to get a reasonable first estimate of the emission landscape

145 using readily available data.

146 **Table 1. Overview of source sectors and subsectors distinguished in the dynamic emission model, including their short**
147 **name used in the figures, whether they are represented as point or area sources, and their approximate contribution to**
148 **the total CO_2 emission in Rotterdam. Crosses indicate which emission factors (EF), and tracer ratios of CO, NOx or**
149 **SO2 (Rco, RNOx, RSO2) are part of the state vector and circles indicate whether they are also part of the short state**
150 **vector (see Sect. 2.3).**

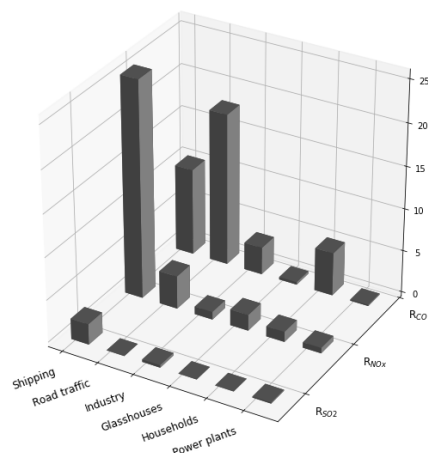| Source sector	Subsector	Short name	Source type	Contribution	EF	R_{CO}	R_{NOx}	R_{SO2}
Power plants	Gas-fired power plants	1A	Point	37 %	XO	X	X	
	Coal-fired power plants	1B			XO	X	X	X
Non-industrial combustion	Households	2A	Area	15 %	XO	XO	X	X
	Glasshouses	2B			XO	X	X	
Industry		3	Point	39 %	XO	XO	XO	XO
Road traffic	Cars	7A	Area	6 %	XO	XO	XO	
	Heavy duty vehicles	7B			XO	XO	XO	
Shipping	Ocean shipping	8A	Area	3 %	XO	X	XO	XO
	Inland shipping	8B			XO	X	XO	XO
	Recreational shipping	8C						

151

152 The emissions are calculated in four steps. First, the yearly, national emission is calculated per sector using

153 reported annual activity data and CO_2 emission factors. Second, we apply temporal disaggregation to hourly

154 emissions using time profiles based on a combination of default temporal profiles, and environmental conditions.

155 Third, we downscale the national totals to 1x1 km^2 resolution using statistical data, such as population density.

156 Finally, our approach also allows uncertainties to be described in detail based on parameters in Eq. (2).

157 **2.1.1 Step 1: Sectorial total emission calculations**

158 Total annual emissions (F_X in kg yr^{-1}) per sector and species (X=CO_2, CO, NO$_x$, SO$_2$) are calculated as a function

159 of the economic activity and an emission factor (adapted from Raupach et al. (2007)):

$$F_X = A \left(\frac{E}{A}\right) \left(\frac{F}{E}\right) R_X \tag{1}$$

161 where A is the amount of activity, such as vehicle kilometres driven or generated power, and E is the primary

162 energy consumption (petajoule (PJ)). R_X is the emission ratio needed to calculate emissions of co-emitted species

163 X from the CO_2 emissions, which is specific for each economic sector (R_{CO_2} is always 1, others are illustrated in

164 Fig. 2). In this equation the term F/E is the emission factor (EF), i.e. the amount of CO_2 emitted per amount of

165 energy consumed. The term E/A can be seen as a measure of energy efficiency, in which technological

166 development plays an important role (Nakicenovic et al., 2000).

Figure 2. Emission ratios of CO:CO$_2$ (R_{CO}), NO$_x$:CO$_2$ (R_{NOx}) and SO$_2$:CO$_2$ (R_{SO2}) for specific source sectors based on the Dutch Pollution Release and Transfer Register (Netherlands PRTR, 2014). Units are in ppb ppm^{-1}. A value of 10 on the y-axis thus implies that for each 1000 moles of CO$_2$, 10 moles of the auxiliary tracer is emitted.

The information needed in Eq. (1) comes from various inventories and national information sources. For example, changes in annual activity can be approximated based on national statistics such as the GDP (Gross Domestic Product), which can be a proxy for industrial activity. Or A can be based on environmental data such as the annual degree day sum based on the outside temperature, as proxy for the need for household heating in a particular year. The second term in Eq. (1) (*E/A,* the energy efficiency) can be estimated from energy consumption statistics, such as available from the International Energy Agency. Note that this term can show a large trend in case of technological development. The last terms in Eq. (1) (*F/E* and R_x, the emission factors) are the most uncertain ones, because the emission factor is dependent on the fuel mix and the energy efficiency, which itself can vary with environmental conditions (e.g. a cold engine on a winter day burns less efficiently). It can therefore differ significantly between countries. Emission factor values that are generally valid can be gathered from the Intergovernmental Panel on Climate Change (IPCC) or the European Environmental Agency (EEA), while country-specific values are typically less easily accessible. For our study area, we have access to both EEA data, as well as to Netherlands-specific numbers and even to Rijnmond-specific values (PRTR). See Appendix A for a full overview of the data used.

2.1.2 Step 2: Temporal profiles and parameterizing activity

The second step is to disaggregate the yearly emissions to hourly emissions by calculating time profiles, such that Eq. (1) becomes "dynamic":

$$F_{X,t} = A\left(\frac{E}{A}\right)\left(\frac{F}{E}\right)R_X T_t \tag{2}$$

where T_t is the hourly time factor. Averaged over a year the value of T_t is 1.0, so that it only alters the temporal evolution and not the total emissions. Energy use is often specifically linked to an activity (*A* in Eq. (1) and Eq. (2)) on which temporal information is more readily available than on the resulting emissions. Therefore, T_t can be calculated in two ways: 1) by directly using temporally explicit activity data or 2) by parameterizing temporal variations from environmental and/or economic conditions. When activity data is available the first option is

7

195   preferable. However, in data-sparse regions the second option might be necessary to implement, which is still an

196   improvement compared to long-term average profiles as commonly used as we will discuss next for several sectors

197   represented in our dynamic emission model.

198   Non-industrial combustion is dominated by households' natural gas consumption to heat houses, for cooking, and

199   for warm water supply. A Dutch energy provider has a dataset publicly available from about 80 smart meters for

200   the year 2013 with hourly gas consumption (Liander, 2018). It clearly shows a seasonal cycle, but also more small-

201   term variations (daily data are shown in Fig. 3). We also see higher gas consumption in the beginning of the year,

202   where the first three months of 2013 had some long, cold spells.

203   The use of energy for household heating is connected to the outside temperature. Previous studies have therefore

204   used the concept of heating degree days to describe the temporal variability in emissions from households (Mues

205   et al., 2014; Terrenoire et al., 2015). This concept assumes that heating only takes place below a certain temperature

206   threshold (here 18°C) and the hourly time factor can be defined as:

207    $T_t = H/\overline{D}$ (3)

208   where H is the heating degree day factor ($H = max(291.15\text{-}\overline{T_{2m}},0)$) based on the daily mean outside temperature

209   at 2 m. $\overline{D}$ is the yearly average heating degree day ($\overline{D} = \frac{1}{N}\sum_{j=1}^{N} H$). However, gas consumption related to warm

210   water supply and cooking is largely independent of the outside temperature and therefore a constant offset is

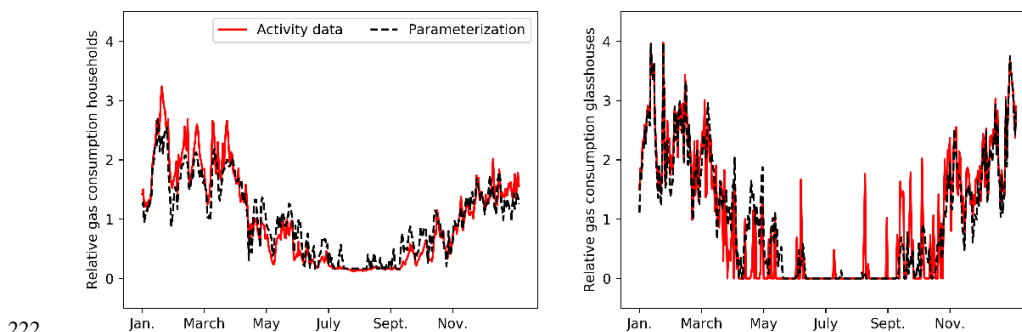211   included in the heating degree day factor:

212    $H_f = H + f \cdot \overline{D}$ (4)

213   where f is the constant offset. We assumed an offset of 20 %, similar to Mues et al. (2014). The time factor can

214   now be defined as:

215    $T_t = H_f/\overline{D_f}$ (5)

216   where the average heating degree day accounted for the constant offset $\overline{D_f} = (1 + f)\overline{D}$.

217   We compared the heating degree day method with gas consumption data on a daily basis (Fig. 3). The degree day

218   function follows the gas consumption data very well, including the higher consumption at the start of the year,

219   reaching an R^2 of 0.90 (N=365). The gas consumption of consumers also has a diurnal pattern with peaks in the

220   early morning and late afternoon. Therefore, a diurnal profile can be estimated based on typical working hours.

221   For hourly data R^2 is 0.80 (N=8760, not shown).

222
223   **Figure 3. Daily time profiles for households (left) and glasshouses (right). Solid red lines are based on true activity data,**
224   **whereas dashed black lines are parameterizations based on the degree day function.**

225   For the energy consumption of glasshouses there is no true activity data available. Instead, we use modelled daily

226   energy consumption for a typical Dutch glasshouse cultivating tomatoes (courtesy of Bas Knoll, TNO) as the

227   'truth' (activity data). This time profile is calculated for typical meteorological conditions, such that the order of

228   magnitude and the peaks are representative for an average year. There is almost no energy consumption during the

229   summer, which indicates that there is no constant offset. So, we use Eq. (3) to determine the emission factor.

230   Moreover, we use a lower temperature threshold of 15 °C to get a better fit with the observed energy consumption.

231   The estimated function compares well with the activity data (Fig. 3) with an R^2 of 0.85 (N=365).

232   The diurnal cycle of glasshouse emissions is likely to be different from that of household emissions. Yet we lack

233   data to establish a diurnal cycle. We therefore use the same diurnal profile as for households, although this is likely
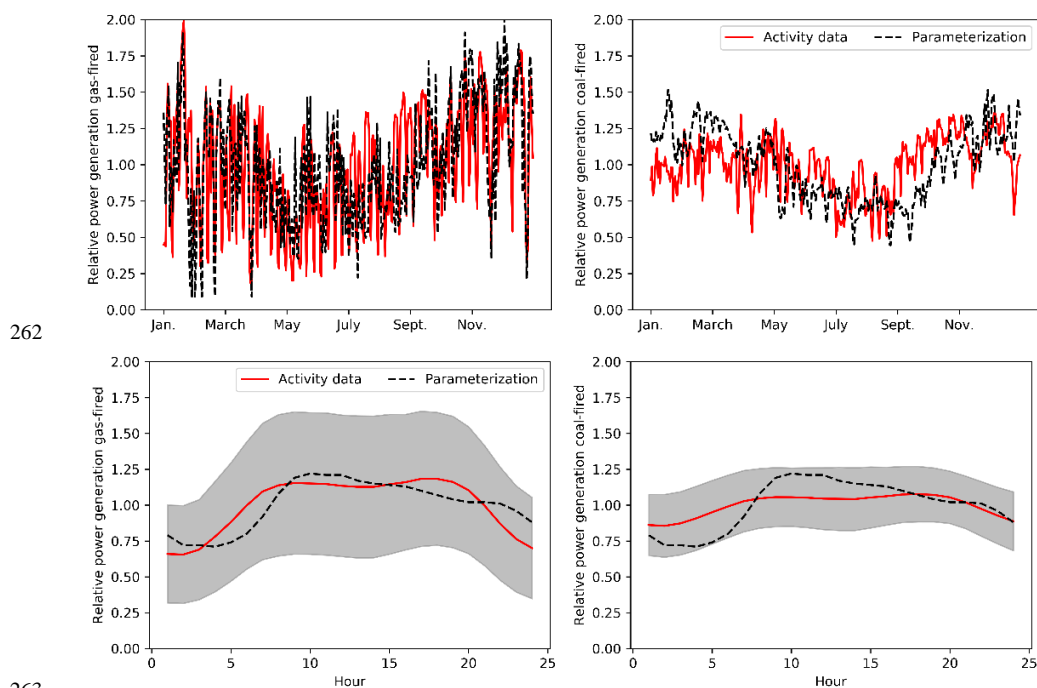
234   to be incorrect.

235   Power plants can use different fuels such as hard coal, natural gas or biomass. In the Netherlands coal-fired and

236   gas-fired power plants account for 80–85 % of the total energy production. The remainder comes mainly from

237   wind energy (5–6 %) and biomass burning (5–6 %). Power generation data are reported by the European Network

238   of Transmission System Operators for Electricity (ENTSO-E), which has detailed data available for the whole of

239   Europe. Coal-fired power plants are currently the main source of energy and their generation is relatively stable

240   compared to other sources. It does, however, show a seasonal cycle with less energy production during the summer

241   months. Gas-fired power plants have a larger temporal variability as they are mainly used as back-up for peak

242   hours, depending also on the amount of renewable energy that is available.

243   We use Eq. (5) to estimate the time profiles of both coal- and gas-fired power plants. Linear regression analysis

244   shows that the coal-fired power generation is correlated with degree days (R^2 = 0.17). In this case we use a large

245   constant offset of 80 % and a threshold of 25 °C which were chosen to best match the actual power generation

246   data. The offset is much larger than for households because there is always a basic energy demand from the

247   industry. In contrast, the gas-fired power plants are (negatively) correlated with the wind speed (R^2 = 0.13) and

248   incoming solar radiation (R^2 = 0.10), indicating the need for gas-fired power generation in the absence of

249   renewable sources. Therefore, we replace the temperature used to calculate H_f in Eq. (4) with the multiplication of

250   wind speed and incoming solar radiation:

251   $$H = \max(10 - \bar{u}, 0) \cdot \max(150 - \bar{R}, 0) \tag{6}$$

252   where u is the wind speed (m s^{-1}) and R the incoming solar radiation (J cm^{-2}). Here we use a constant offset of 10

253   % and a threshold of 10 m s^{-1} and 150 J cm^{-2}.

254   The diurnal cycles for power plants can be based on socio-economic factors. For example, the energy demand

255   peaks early in the morning when people get ready to go to work and at the end of the afternoon when they get

256   home. We find this pattern in the actual power generation data, with coal-fired power plants being less variable

257   during the day than gas-fired power plants. The fixed profile from the European MACC-III emission inventory

258   (Denier van der Gon et al., 2011; Kuenen et al., 2014) matches reasonably well with gas-fired power plant profiles,

259   but it is less applicable for coal-fired power plants (Fig. 4). Overall, the estimated profiles for gas-fired power

260   plants (hourly data) have an R^2 of 0.32 (N=8784) when compared to the activity data. For coal-fired power plants
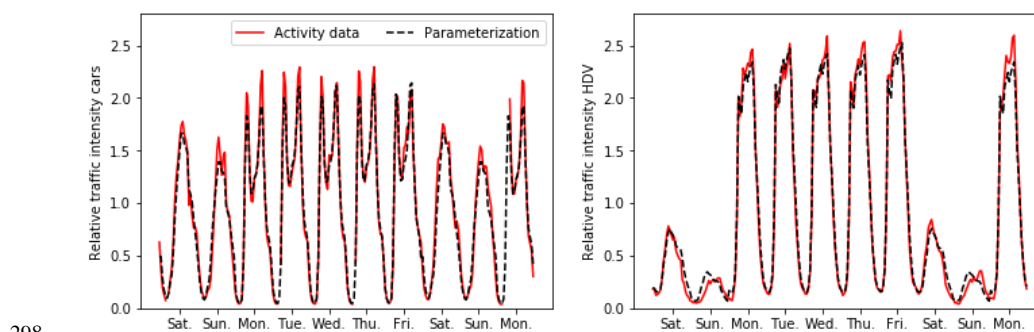
261   this is 0.21 (N=8784).

262

263

Figure 4. (top row) Daily time profiles for gas-fired (left) and coal-fired (right) power plants. Solid red lines are based on true activity data, whereas dashed black lines are parameterizations based on observed temperature (coal) and wind speed/radiation (gas). (bottom row) Average diurnal cycle for gas-fired (left) and coal-fired (right) power plants. Solid red lines are based on true activity data, whereas dashed black lines are fixed profiles from the MACC inventory (Denier van der Gon et al., 2011; Kuenen et al., 2014). Shading gives the 1σ variability of the diurnal cycle based on activity data.

270 The industrial sector consists of a wide range of activities, of which some are semi-continuous and only interrupted

271 by maintenance stops while others follow working hours. This makes it very difficult to predict the temporal

272 variability, especially for the overall sector. Since the largest CO_2 emissions are related to refineries and heavy

273 industry we will focus on these activities. We find a seasonal cycle in the reported industrial activity, with a small

274 decline during the summer and Christmas holidays. However, the variations are very small (max. 1 %). Therefore,

275 we assume constant emissions.

276 Road transport emissions can vary between different road and vehicle types (Mues et al., 2014), but are also

277 strongly dependent on environmental, socio-economic and driving conditions (such as the amount of stops, free-

278 flow versus stagnant conditions, and engine temperature). Traffic count data are often used to create average time

279 profiles for road traffic emissions, although with traffic counts we are unable to account for environmental and

280 driving conditions. Traffic counts for the Netherlands are made available by the Nationale Databank

281 Wegverkeersgegevens (NDW) and similar data is available in many developed countries. We differentiate between

282 two vehicle types (passenger cars + motorcycles (hereafter referred to as cars) and light duty + heavy duty vehicles

283 (hereafter referred to as HDV)) and three road types (highway, main road, urban road). We selected all available

284 locations for 2014 within or close to Rotterdam that distinguish 3-5 vehicle lengths and filtered for a minimum

285 data coverage of 75 %. This leaves us with 25 highway, 6 main road and 13 urban road locations. From this data

286 we make average time profiles (daily, weekly and monthly) per road and vehicle type, as is often done to

287 disaggregate road traffic emissions. Note that this method excludes any spatial variations (e.g. highways leading

288 towards the city vs. the beach), except for differentiating between road types.

289 Generally, HDV show a larger spread due to the low counts during the weekend (Fig. 5). Car counts on weekdays

290 show a morning and evening rush hour and they go down in between. In contrast, HDV counts peak throughout

291 the day and only go down after the evening rush hour. Moreover, the diurnal cycles are different during the

292 weekend than on weekdays. These patterns can be explained from socio-economic factors. Current time profiles

293 are often based on cars and are unable to correctly represent the temporal variability of HDV. This also affects the

294 spatial distribution of emissions and therefore we create average diurnal, weekly and seasonal profiles separately

295 for cars and HDV, for different road types and considering the day of the week. The comparison of true traffic

296 counts and averaged traffic counts results in R^2 values between 0.83 and 0.95 for hourly data for the whole year
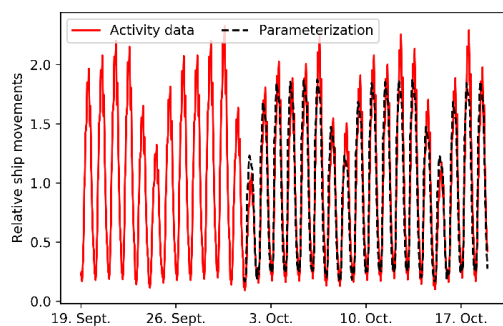
297 (N between 2665 and 6471).

Figure 5. Time profiles of passenger cars (left) and heavy-duty vehicles (right) road transport on highways for ten randomly chosen days in March. Solid red lines are based on true activity data, whereas dashed black lines are parameterizations based on averaged traffic counts for Rotterdam.

302 Shipping emissions are dependent on the type of fuel used and whether ships apply slow-steaming. Additionally,

303 during loading and unloading ships still emit CO_2 and other pollutants, even though they are not moving. Such

304 information is currently not available, so instead we use information about the arrival and departure of ships in the

305 port of Rotterdam to make a time series of ship movements. Note that this only applies to large vessels that

306 transport goods and passengers and that the time profile will look quite different for recreational shipping.

307 However, large ships account for approximately 80 % of the total shipping emissions in the area of interest. Since

308 we lack information about other type of shipping movements, we will only account for large ships in the time

309 profiles.

310 We collected ship movements for one month (daily data) and an average diurnal profile. The diurnal cycle shows

311 a peak throughout the day, which corresponds well with the HDV road transport emission patterns on highways.

312 The reason for this is that HDV road transport is related to shipping movements, as HDV takes care of part of the

313 good transport further inland after the goods have arrived by ship. We also find a clear weekly pattern with less

314 ship movements during the weekend, although the decrease is less than for HDV road transport. This is likely

315 because large ships, such as entering the port of Rotterdam, continue travelling during the weekend. Therefore,

316 the weekly pattern resembles more that of car road transport on highways. Thus, we can estimate ship movements

317 by using the temporal profiles of HDV and cars on highways. This method is specifically tested for Rotterdam and

318 different patterns might be visible elsewhere. We also use HDV patterns for the seasonal variability, and final

319   parameterized and reported activity in this method reach an R^2 value of 0.89 for a period of 18 days with hourly

320   data (N=432) as shown in Fig 6.

321

322   **Figure 6. Daily time profiles for shipping. Solid red line is based on true activity data, whereas dashed black line is a**
323   **parameterization based on traffic counts of heavy-duty vehicles (diurnal cycle) and cars (day-to-day variations) on**
324   **highways.**

325   **2.1.3 Step 3: Spatial disaggregation.**

326   National total sectorial emissions need to be distributed into spatially explicit emissions for our study domain. The

327   spatial disaggregation of emissions has received quite some attention already from inventory builders. Existing

328   emission inventories can be used to describe the spatial disaggregation, if available for the region at high

329   resolution.

330   If not, simple default proxies for the spatial distribution are population density and the presence of roads or

331   waterways (e.g. OpenStreetMap). For example, main roads and urban roads are busiest in densely populated areas

332   and we assume emissions on main and urban roads are correlated with population density. Highways are used for

333   transport between cities and therefore emissions take place outside densely populated areas as well. Nevertheless,

334   highway transport is usually to and from densely populated areas, such that most emissions will take place close

335   to cities. We can therefore relate these emissions with the population density in the area of interest (in this case

336   Rijnmond) relative to the rest of the country, which places the same amount of the country-level emissions in our

337   case study domain as the gridded inventory. Additionally, the location of large power plants or industrial plants is

338   often known (for example from E-PRTR (Pollutant Release and Transfer Register), which can be used directly.

339   Although such information allows us to possibly construct a detailed fossil fuel model in data-sparse regions in

340   the future, in this study we focus first on the more easily implementable and less-developed parameterization of

341   temporal activity in different sectors (step 2) to assess whether this approach is promising enough for future

342   extension.

343   **2.1.4 Step 4: Uncertainty analysis**

344   The emission model we have constructed in steps 1–3 contains several parameters per source sector: activity,

345   emission factor, spatial proxy and time profile. For the analysis we only consider the emission factors and time

346   profiles, as we assume activity data and the spatial distribution to be well-known. As input for step 1 in the dynamic

347   emission model we use generalized parameters which we take from the IPCC, EEA and other organizations. These

348   databases also provide an uncertainty range, which we use in a final step to create a covariance matrix. The

349   covariance matrix describes the Gaussian uncertainty of these parameters (diagonal values) and error correlations

350   between parameters (off-diagonal values). From the covariance matrix we create an ensemble of parameters

12

351   (N=500) that represents their joint distributions, and we use them to calculate an ensemble of emissions. In this

352   Monte Carlo simulation, we transform some Gaussian parameters into log-normal distributions to account for non-

353   negativity, or to account for distributions with a very long tail (mainly emission ratios, which can become high in

354   specific cases where no emission reduction measures are taken). Appendix A summarizes the used parameter

355   values and uncertainties (including the shape of the distributions) and shows an example of the covariance matrix.

356   In a final step, we select the most important parameters which are either very uncertain or have a large impact on

357   the total emissions. This leaves us with the 44 parameters that we optimize in a set of data assimilation experiments,

358   described next. In Sect. 3.1 we report uncertainties in % (1 σ) for normal distributions (CO_2) or as a 90 %

359   confidence interval (CI) for lognormal distribution (co-emitted species).

2.2 Data assimilation to estimate fossil fuel sources

361   The goal of data assimilation is to find a state at which the system is in optimal agreement with observations. In

362   this work, the observations we want to explore are the mole fractions of CO_2 and its co-emitted species while the

363   state of the system is the underlying spatiotemporal distribution of fossil fuel emissions. Such configurations are

364   sometimes referred to as "FFDAS" (fossil fuel data assimilation systems) applications, with a number of examples

365   in recent literature (Rayner et al., 2010; Asefi-Najafabady et al., 2014; Basu et al., 2016; Graven et al., 2018).

366   Given the sparsity of approaches explored so far, the dynamic emission model with its parameter driven emissions

367   we present here could lend itself well for application in an FFDAS, and this is what we explore through a set of

368   experiments with our own data assimilation methodology.

369   In this study we use the CarbonTracker Data Assimilation Shell (CTDAS) (v1.0) described in detail in Van der

370   Laan-Luijkx et al. (2017). Briefly, the CTDAS system is a flexible implementation of a square-root Ensemble

371   Kalman Filter (Whitaker and Hamill, 2002), which also allows lagged windows (i.e. smoothing instead of

372   filtering). The Ensemble Kalman Filter optimizes the cost function for unknown variables in the state vector x

373   using information from observations (y^0 with covariance R) and a prior estimate of the state vector (x^b with

374   covariance P).

375   $$J(x) = \left(y^0 - \mathcal{H}(x)\right)^T R^{-1}\left(y^0 - \mathcal{H}(x)\right) + (x - x^b)^T P^{-1}(x - x^b) \tag{7}$$

376   In this function, $\mathcal{H}$ is the observation operator that returns simulated mole fractions given the state vector. R and

377   P determine how much weight is given to the observations and prior estimate, respectively.

378   The optimized state vector (indicated with superscript a, whereas b refers to the prior estimates) which minimizes

379   the cost function is

380   $$x^a = x_t^b + K(y_t^0 - \mathcal{H}(x_t^b)) \tag{8}$$
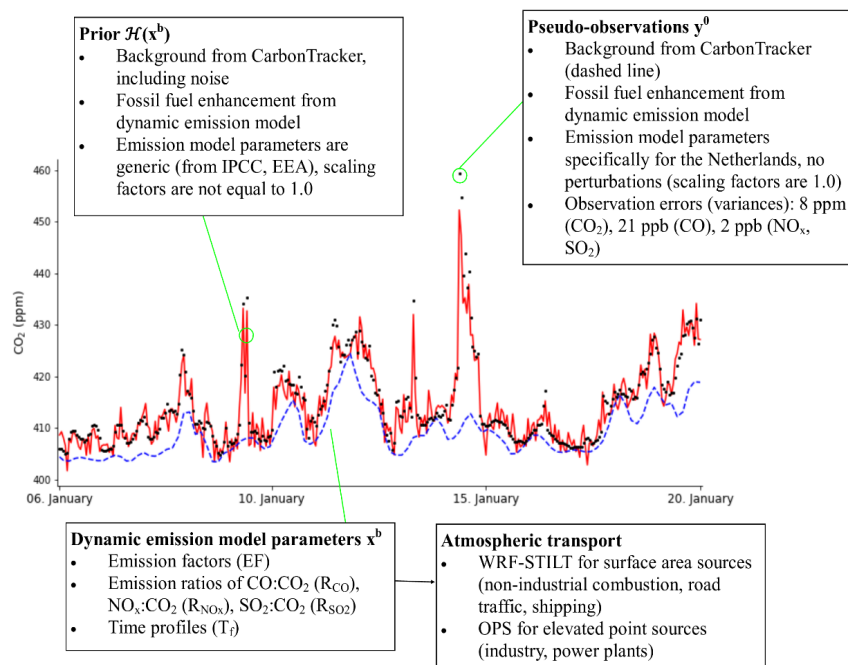
381   and its covariance is

382   $$P_t^a = (I - KH)P_t^b \tag{9}$$

383   Here, H is the linearized observation operator and K is the Kalman gain matrix:

384   $$K = \left(P_t^b H^T\right)\left(H P_t^b H^T + R\right)^{-1} \tag{10}$$

385   The solutions of Eq. (8) and Eq. (9) are calculated as in Peters et al. (2005) using an ensemble of 80 members. The

386   choice for the ensemble size was based on the typical dimensions of our inverse problem, which has N=1960

387   observations and M=44 unknowns for the base run.

Figure 7. Time series of pseudo-observations and prior CO₂ mole fractions and a summary of how these time series were created.

391   We have adapted CTDAS for smaller scale studies by replacing the typical observation operator $\mathcal{H}$, which is the

392   global TM5 transport model (Huijnen et al., 2010), with a combination of WRF-STILT footprints and the OPS

393   plume model, building on the methods described in Super et al., (2017a) and He et al. (2018). Moreover, we have

394   added our dynamic emission model to the observation operator so that we can sample its parameter distribution in

395   atmospheric mole fraction space. More details about the individual parts of this system are provided below and

396   are summarized in Fig. 7.

2.2.1 Observation operator

398   The observation operator translates the 44 parameters in the dynamic emission model first into emissions (through

399   Eq. (1) and Eq. (2)) and then into atmospheric mole fractions. The transport modelling consists of two parts. The

400   first part, the Weather Research and Forecasting-Stochastic Time-Inverted Lagrangian Transport (WRF-STILT,

401   (Nehrkorn et al., 2010) model, is used for surface emissions that are representative of large areas (i.e., not a point

402   source). STILT is a Lagrangian particle dispersion model that describes the footprint of a single measurement by

403   dispersing particles back in time (Gerbig et al., 2003; Lin et al., 2003). With this footprint the surface influence of

404   emissions on a single observation can be described. An advantage of this method is that it allows the pre-

405   calculation of linear atmospheric transport, which makes this part of the observation operator less computationally

14

406   demanding than running an ensemble of a full atmospheric transport model (like WRF with chemistry). The total

407   domain covered with WRF-STILT is 77 x 88 km (Fig. 1) and includes most of the Randstad.

408   To generate a footprint, 75 particles are released at the observation site at the start of the back-trajectory and

409   followed back in time. Given that the variability in hourly observations at an urban location is dominated by local

410   signals, we construct back-trajectories spanning 6 hours. This is based on the domain size, which could be covered

411   within 6 hours for typical wind speeds of 4 m s^{-1}. Within this time frame emissions can become well-mixed

412   throughout the boundary layer under normal daytime mixing conditions, such that emissions outside this range

413   can be represented by a boundary inflow. Footprints are generated for each hour within the back-trajectory to

414   account for hourly variations in the emissions. We drive STILT with meteorology from the WRF model (v3.5.1).

415   The WRF model was set up with two nested domains (15x15 and 3x3 km^2 horizontal resolution) and the STILT

416   footprints have a 1x1 km^2 resolution over the entire domain.

417   The second part of the transport modelling is a plume model. In a previous study we have shown that point source

418   (stack) emissions should be modelled with a plume model to better represent the limited dimensions of the stack

419   plume (Super et al., 2017a). Similarly, Vogel et al. (2013) have shown that the surface influence calculated by

420   STILT can lead to large model errors for stack emissions. Therefore, we include the OPS (Operational Priority

421   Substances, short-term version) plume model in our framework to model the transport and dispersion of stack

422   emissions (Van Jaarsveld, 2004; Sauter et al., 2016). OPS provides hourly concentrations at pre-defined receptor

423   points, which represent our measurement sites. The model keeps track of a plume trajectory, considering time-

424   varying transport over longer distances (e.g. changes in wind direction and dispersion). If for a time step a specific

425   plume affects the receptor, a Gaussian plume formulation is used to calculate the mole fraction caused by that

426   source based on the true travel distance along the trajectory. We drive the model with the same WRF meteorology

427   as STILT. Only primary meteorological variables (temperature, relative humidity, wind direction, wind speed,

428   precipitation, global radiation) are prescribed, secondary variables (e.g. boundary layer height, friction velocity)

429   are calculated by OPS itself and can differ from WRF.

430   Similar to the WRF-STILT model, we assume an influence time of 6 hours on our observations. However, in this

431   case we run the OPS model forward from -6 hours to the time of observation. We apply the OPS model only to

432   point source emissions within the Rijnmond area, as we found in a previous study that a plume model only has an

433   added value less than 10–15 km downwind from the stack (Super et al., 2017a). Point sources at more than 10–15

434   km from the observation site can be sufficiently represented with a Eulerian model. The OPS model input includes

435   detailed information about the exact stack height and heat content of the plume.

436   In addition to the fossil fuel contribution we also include background mole fractions for CO_2 and CO. NO_x and

437   SO_2 are short-lived and therefore the variations in the background are relatively small compared to the fossil fuel

438   signals. The CO_2 background is taken from the 3-D mole fractions of CarbonTracker Europe (Peters et al., 2010)

439   and also accounts for biogenic fluxes. The resolution of these CO_2 fields is 1x1° and we select the grid box that is

440   situated over Rotterdam. The 3-hourly data are linearly interpolated to get hourly background mole fractions that

441   are added to the fossil fuel signals calculated by the transport models. We use the strong wintertime correlation

442   between CO_2 and CO mole fractions (r = 0.73) to calculate CO background conditions from the CO_2 background.

443   This is not very accurate, but for the purpose of this OSSE it provides us with a decent estimate of the variability

444   in background mole fractions.

445   **2.2.2 State vector**

15

446   We populated the state vector with a selection of the most important parameters of the dynamic emission model,
447   based on their impact on the total emission uncertainty described in the results (Sect. 3.1). However, we
448   hypothesize that emission model parameters that are not part of the state vector are nevertheless uncertain and may
449   affect the results. Therefore, we include a total of 44 scaling factors in our state vector (x^b), and each scaling factor
450   is linearly related to a parameter from the dynamic emission model. The uncertainty in these parameters
451   (covariance matrix P) is derived from the Monte Carlo simulations described in Sect. 2.1, with the spread in the
452   emission model parameter values provided by the same databases of the IPCC and EEA. These uncertainty values
453   can also be found in Appendix A.

454   For this study we selected an arbitrary two-week period in January 2014 (6–20 January). Note that during the
455   summer the importance of source sectors might be different, e.g. there will be less heating from households.
456   Nevertheless, this period is sufficient to test the applicability of our DA system. We loop over the 14 days in our
457   study period, resulting in one posterior state vector for each day. We initialize our state vector for every new day
458   using the posterior values and posterior uncertainties from the previous day. Because the footprints we generated
459   extend backwards for six hours, the state vector for each day is effectively only constrained by the observations
460   from that same day, and hence we did not use a Kalman-smoother approach in this work in contrast to other
461   CTDAS applications.

462   Although this is a data-rich region, we use generic values for the prior emission model parameters which we take
463   from the IPCC, EEA and other organisations (Appendix A). These values are typically valid for a large region
464   (e.g. Europe) and not necessarily the best estimate for our regional case study. The reason that we use these values
465   is that they can provide a first estimate of the emissions in data-scarce regions where inverse modelling might add
466   most to our knowledge. With this set-up we can examine how well we can constrain the true emissions starting
467   with this generic, and widely available, information.

468   One major challenge in this study is to attribute the mismatch between the observed and modelled mole fractions
469   to a specific sector, as a CO_2 observation alone provides no details on the origin of the CO_2. Therefore, we include
470   three tracers (CO, NO_x and SO_2) that are co-emitted with CO_2 during fossil fuel combustion in a ratio (referred to
471   as R_{CO}, R_{NO_x} and R_{SO2}) that is specific for each source sector (Fig. 2). Their (pseudo-)observations can inform us
472   about the source of the mismatch, but through their emission ratio to CO_2 they also constrain the magnitude of
473   CO_2 emissions in the emission model. The ratios R_{CO}, R_{NO_x} and R_{SO2} used for this conversion to CO_2 emissions is
474   not fixed: for each of the co-emitted species we included them in the state vector. This recognizes that emission
475   ratios are highly variable and uncertain but play an important role in source attribution.

2.2.3 Pseudo-observations

477   In this work we create observing system simulation experiments (OSSEs), which use pseudo-observations instead
478   of true observations. The advantage of using pseudo-observations is that we can accurately examine the abilities
479   of our new approach without having to account yet for (often dominant) atmospheric transport errors.

480   The pseudo-observations used to optimize the emission model parameters are created using the same observation
481   operator as described above. The dynamic emission model is used to create realistic emissions with a high
482   spatiotemporal resolution. Yet in contrast to the prior, we use specific local (Dutch) values for the emission model
483   parameters. These parameters are considered to be the truth and are therefore not scaled (scaling factors are 1.0).
484   We found that these local parameter values are always within the uncertainty range of the general (prior) values,

485 so that the true solution is part of the distribution explored within the prior. This is confirmed in an experiment

486 with a small model-data mismatch and no noise on the background, which reproduces the true parameters very

487 well (not shown).

488 The resulting emissions are used in combination with the background mole fractions and transport calculated by

489 WRF-STILT and the OPS model to create pseudo-observations at the locations shown in Fig. 1. For the pseudo-

490 observations the original background time series are used, whereas in the inversion random noise is added to the

491 background mole fractions with a standard deviation of 2 ppm for CO_2. We assume no contribution from biogenic

492 CO_2 to the excess CO_2 over the background, which means that any biogenic contribution to CO_2 within our

493 footprint is the same as in the inflow from outside our domain, thus cancelling in the subtraction of the background

494 CO_2.

495 One simulated time series is illustrated in Fig. 7. The monitoring network consists of seven sites that are scattered

496 over the city of Rotterdam and the port. All sites exist in the national CO_2 or air quality measurement networks,

497 although not all species used in the inversion are observed at all locations. We only use the daytime (12–16 h LT)

498 observations to constrain our emissions. This is normally done to favour well-mixed conditions when simulated

499 transport is more reliable, and we want to mimic this limitation. We assume all instruments have an inlet at 10m

500 above ground level. In reality this is lower for several sites, but during the well-mixed daytime conditions the

501 difference is minimal.

502 The covariance matrix R describes the observation error. It accounts for errors related to instrumentation, but also

503 representativeness errors due to model transport, interpolation, and parameterization used in the dynamic emission

504 model. Although in principle such errors can be excluded in an OSSE, we prefer to use realistic estimates of these

505 errors to allow for the random errors that we applied to the prescribed boundary inflow, as well as to account for

506 some parameters in the emission model that are not optimized even though they contained uncertainty in the

507 pseudo-data creation. We base the R matrix on the calculated errors and variability caused by these specific

508 differences, and we end up with variances of 2.5 ppm (CO_2), 8 ppb (CO), 3 ppb (NO_x) and 1 ppb (SO_2).

509 **2.3 Data Assimilation Experiments**

510 We perform various experiments to examine the sensitivity of the system to different set-ups and sources of error.

511 The experiments are discussed here, and the detailed set-up of the inversions is summarized in Table 2. The base

512 run is labelled "Base".

513 1) State vector definition: We start with a comparison of two different state vectors. For this purpose, we compare

514 the base run with an inversion (Short_state) which only includes the 21 most important parameters as identified in

515 the sensitivity analysis. This test allows us to examine the impact of erroneous, non-optimized emission model

516 parameters on the emission estimates. The results are discussed in Sect. 3.2.

517 2) Source attribution: Next we compare two monitoring network configurations which differ in the number of

518 tracers used. We perform an inversion with CO_2 as the only tracer (CO_2_only) and one with the full range of tracers

519 (Base) to assess the added value of including co-emitted species for source attribution. These tests address the

520 question whether co-emitted species can be used for source attribution. The results are discussed in Sect. 3.2.

521 3) Propagation: The third experiment is used to examine the effect of propagation of posterior values and

522 uncertainties on the final emission estimates. We compare the base run to a run that has no propagation

523 (No_propagation and CO_2_only_no_propagation) but instead starts from the same prior mean and uncertainty on

17

524 each of our 14 days considered. The runs without would allow the parameter values to change over time. The

525 results are discussed in Sect. 3.3.

Table 2. Overview of the inversions: which tracers are included, the length of the state vector and whether posterior values and uncertainties are propagated.

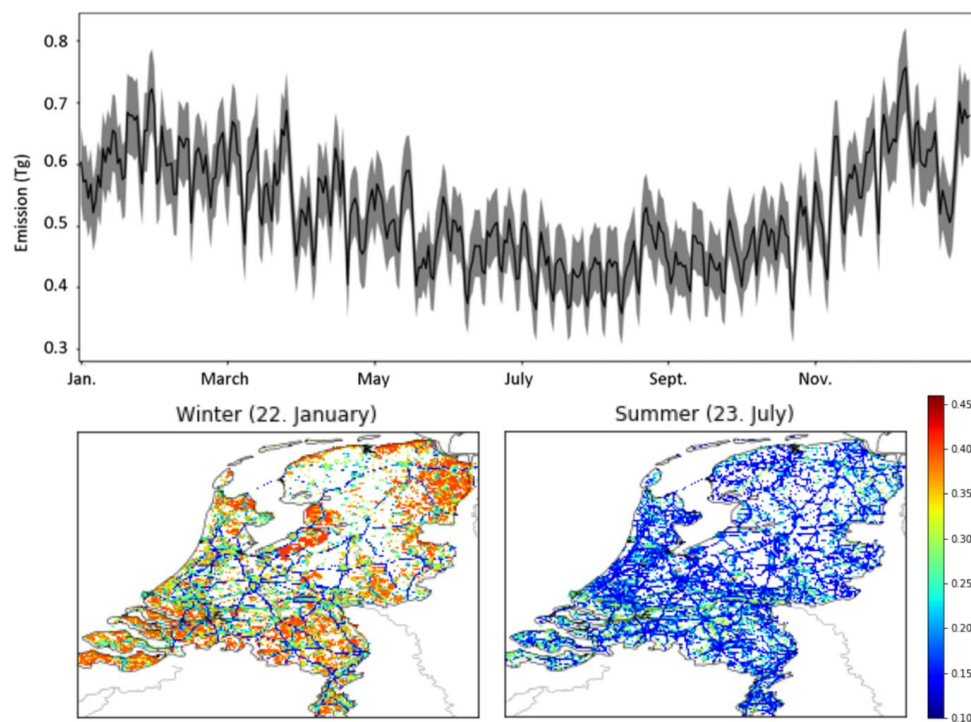| Inversion name	Tracers	State vector length (per day)	Propagation to the next day
Base	All	44	Yes
Short_state	All	21	Yes
No_propagation	All	44	No
CO_2_only	CO_2	44	Yes
CO_2_only_no_propagation	CO_2	44	No

3 Results

529 Before demonstrating the use of our dynamic emission model in an inverse framework, we demonstrate its

530 application as a simple but versatile method to generate hourly gridded emissions for multiple species with full

531 covariances.

3.1 Dynamic emissions and their uncertainty

533 The total yearly emission of CO_2 for the Netherlands calculated with the dynamic emission model is 180 Tg CO_2

534 with an uncertainty of 15 % (1-sigma Gaussian based on 500 members of a Monte Carlo simulation). This matches

535 the total of the Dutch national emission inventory for 2014 by design (step 1), but the uncertainty on the latter was

536 estimated with a similar Monte Carlo simulation to be only 1 % for CO_2 in 2004 (Ramírez et al., 2006). This

537 smaller uncertainty is fully due to the use of country-specific emission factors with a much smaller range than we

538 derived from the IEA and IPCC inventories. Spatial disaggregation (step 2) does not affect the uncertainty of the

539 domain aggregated annual fluxes, and the time profiles (step 3) have no impact on the yearly total emissions. For

540 CO, NO_x and SO_2 the uncertainties in the dynamic emission model are much larger, with medians (CI's) of 6.5×10^8

541 (1.3×10^8–6.8×10^9) kg CO yr^{-1}, 5.0×10^8 (1.2×10^8–5.1×10^9) kg NO_x yr^{-1}, and 1.3×10^8 (5.1×10^6–2.2×10^{10}) kg SO_2 yr^{-1}

542 ^{1}. These ranges result from uncertainties in the assumed ratios of their release per unit of CO_2 emitted.

543 Below the annual scale, time profiles have an impact on the uncertainties as well. The daily emissions of the

544 Netherlands depend on the day and the season (Fig. 8) and range from 0.36 to 0.76 Tg CO_2 day^{-1}. The time series

545 shows a seasonal cycle with lower emissions during the summer. There is a clear weekly cycle with reduced

546 emissions during the weekend. The uncertainty in the total daily emission varies between 8 and 15 %, which is

547 similar to or lower than the uncertainty in the yearly total emissions. The explanation for these relatively low

548 uncertainties is that many uncertainties are temporally uncorrelated and their impacts on individual days partially

549 cancel out. Moreover, the largest sectors (coal-fired power plants and industry) already have a large uncertainty

550 and adding more uncertainty through the time profiles has little impact. Nevertheless, the uncertainties introduced

551 through the time profiles cause an uncertainty in daily CO_2 emissions of about 7 %, if the other uncertainties are

552 excluded from the analyses.

18

553

Figure 8. (top) Time series of daily CO_2 emissions (in Tg CO_2 day^{-1}) and their uncertainty. Given is the interquartile range (shaded area) and the median (line) from the ensemble. (bottom) Map of annual mean relative uncertainty of emissions for the top 25 % pixels with the largest emissions, during a winter month (dominated by household gas- and electricity use) and a summer month (electricity and road-traffic dominated).

Differences in the relative contribution of different sectors are evident when looking at the map of uncertainties across the Netherlands (Fig. 8), reflecting both the most uncertain parameters, but also the dominant source sectors. Winter emissions for example are dominated by household gas-usage, while industrial and traffic emissions give rise to uncertainty year-round at a 10–30 % level. We further identified the most important parameters per source sector with a Monte Carlo simulation per source sector (Fig. 9). Results shows that the road traffic and shipping sectors contain the smallest relative uncertainties, although the time profile for shipping causes an uncertainty of about 7 % in the total shipping emissions. The industrial emissions are most uncertain, and this is almost exclusively due to the emission fact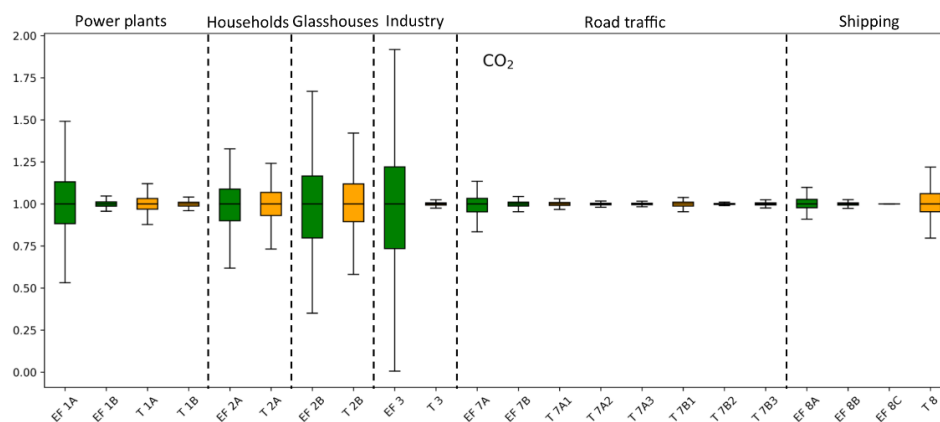or, which causes an uncertaint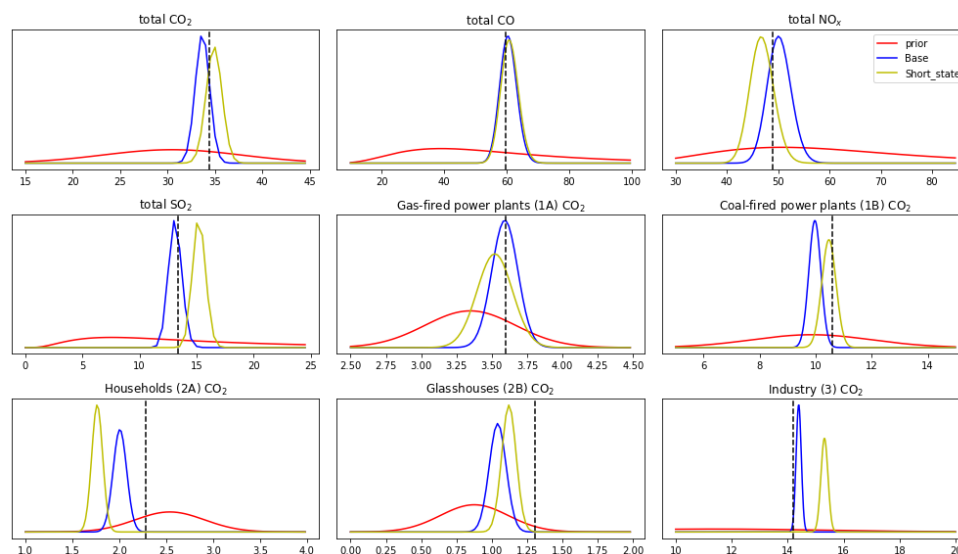y of 41 % in the total industrial emissions. Similarly, the power plant emissions have a large relative uncertainty due to the uncertain emission factor of coal-fired power plants (19 %). Also, for households and glasshouses the emission factor is uncertain (14 % and 26 %, respectively), but here the time profiles also have a large impact (10 % and 16 %, respectively).

19

Figure 9. Box plots showing the uncertainty in the CO_2 emissions from power plants (1A+1B), households (2A), glasshouses (2B), industry (3), road traffic (7A+7B) and shipping (8A+8B+8C) caused by individual parameters affecting that sector. Uncertainty is represented as the spread in daily (normalized) emissions from each ensemble member (N=500) over a full year (N=365). EF refers to an emission factor (green bars) and T to a time profile (orange bars). (Sub)sectors are indicated with their short names as summarized in Table 1. Note that the time profiles of road traffic emissions are specified per road type (1 = highway, 2 = main road, 3 = urban road). Minor parameters that have very small impacts on CO_2 emissions are not shown here (23 out of 44).

3.2 Optimizing dynamic emissions

In the base inverse modelling setup, our system is able to improve the mean estimate and reduce the uncertainty on total CO_2, CO, NO_x, and SO_2 emissions. Figure 10 shows the probability density function of these estimated total emissions, compared to the prior (using parameters derived from IPCC/EEA) and the truth (created with country-specific parameter values). Interestingly, the posterior result deteriorates slightly when using a shortened state vector in which 11 parameters of "minor" influence (such as the SO2:CO_2 ratio of household emissions) are not optimized from their incorrect prior. This is caused by sporadic atmospheric signals that are dominated by household emissions, even if these emissions only contribute a small fraction to the total emissions. These signals are then used to update the emission factor, while the emission ratios are also incorrect.
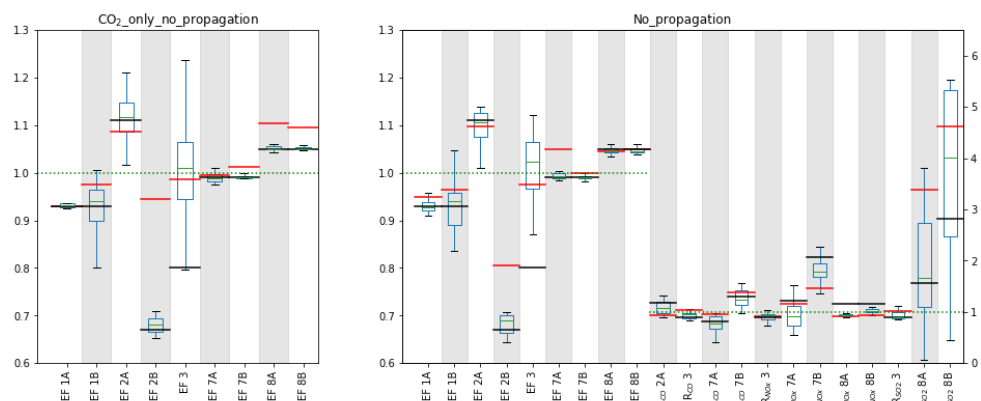
Figure 10. Probability density functions of emissions per species or per source category (for CO_2) in units of Tg (CO_2) or Gg (CO, NOx, SO2). The truth is shown as a vertical dashed line, typically well-matched by the mean of the posterior in blue. Using a shortened state vector (yellow) deteriorates the total non-CO_2 emissions substantially and leads to misattribution of CO_2 emissions in minor categories such as 2A (households).
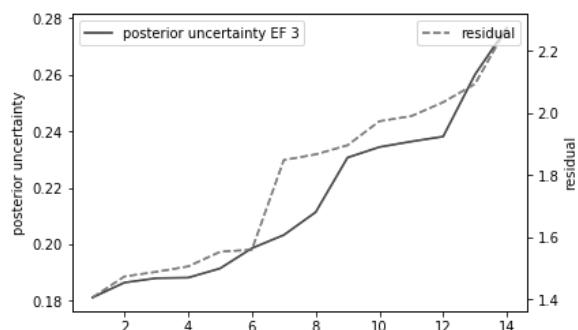
With CO_2 as the only tracer in the inversion we find that we can still estimate total CO_2 emissions quite well (truth-minus-optimized = 0.03 Tg CO_2 yr^{-1}), but we lose the capacity to attribute emissions to specific sectors. Instead, mainly the emission factor of the largest single source being industry (EF3) is optimized. We illustrate this in Fig. 11, using the No_propagation run. The large spread across the 14 individual days indicates that the emission factor jumps around within a large prior uncertainty distribution and is not well-constrained on each day. Some of the other emission factors show almost no deviation from the prior and little variability. Given the constraints posed by CO_2 observations alone, and the limited number of parameters that change the simulated CO_2, optimizing EF3 improves the results at the lowest costs. Introducing the co-emitted species allows the system to identify the source of a residual, and attribute it to the right parameters if sufficient sensitivity is present. This is especially true for those sectors that have relatively small emissions and/or uncertainties, like 2B and 1A. This is corroborated by the posterior covariance matrices (See Appendix B) which show a reduction in parameter correlations for those parameters (i.e., a better mathematical separation of the estimates) when all tracers are included in the estimate. For other parameters the median values are further from the truth than the prior (e.g. for R_{SO2} 8), which indicates that there is too little sensitivity to these parameters.

21

Figure 11. Spread (Q1-Q3) and median values of the parameter scaling factors for the fourteen individual days included in the CO₂_only_no_propagation (left) and No_propagation (right) inversions, and final value of the CO₂_only (left) and base (right) inversion (red lines). The prior values are indicated by the black lines and the truth is indicated with the green dotted lines (value of 1.0). The left y-axis is for the emission factors, the right y-axis for the tracer ratios. The inversion with all tracers shows more variability in the emission factors and larger deviations from the prior values.

3.3 Localization and propagation of information

Propagating information on parameter values from one day to the next is often better than using the median of individual days' estimates as illustrated by the red lines in Fig. 11. Nevertheless, the sporadic detection of plumes with specific signatures suggests that a form of selection or localization of the strongest signals could reduce noise and improve the estimate for the No_propagation run. We therefore ranked the 14 daily independent parameter estimates based on their relative posterior uncertainty and the residuals in an attempt to find the most trustworthy parameter values. This ranking is done per parameter, so the best estimate of different parameters can be related to different days. The increase in residual (same for all parameters) and posterior uncertainty (of the industrial emission factor) is shown in Fig. 12, where the 3–5 highest ranked days have similar characteristics after which the reliability decreases. On the lower ranked days, atmospheric signals from that particular source sector are too small (or even absent) to update the parameters related to that source sector. A similar pattern is found for the other parameters (not shown), with 2–5 days of high sensitivity out of 14.
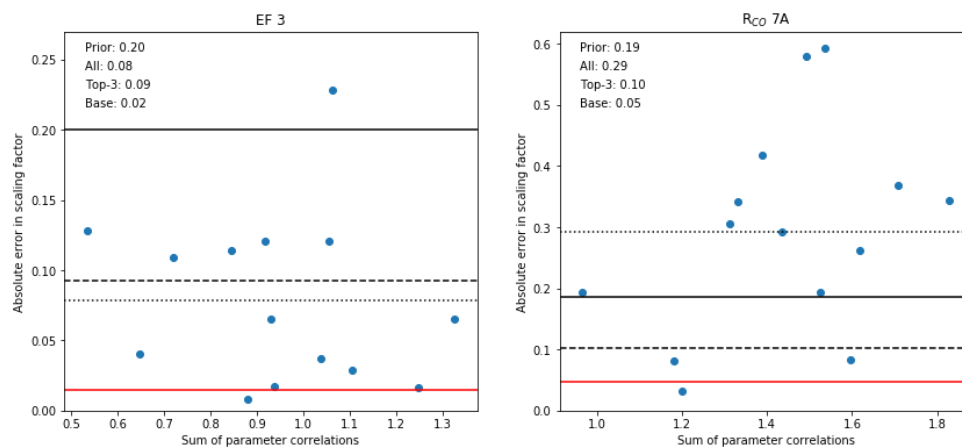

Figure 12. Increase in posterior uncertainty (1σ of unitless scaling factor) in the industrial emission factor (EF 3) and absolute mean residual of CO₂ (in ppm) from highest- to lowest-ranked days.

628 When we use the top-3 averaged parameter values to calculate emissions we find for most sectors that the emission
629 estimate is similar to the base run, albeit with a larger uncertainty, while for a few specific sectors results
630 deteriorate. This suggests that selecting for strong signals can dampen spurious noise, but still does not improve
631 on the base run that includes full propagation of the covariances, hence carrying information on parameter
632 correlations that is partially lost in the No_propagation run.

633 From the posterior covariance matrices we can confirm our selection of "good" days, as these typically show
634 relatively weak correlations between parameters. For the industrial sector (emission factor, R_{NOx}, R_{SO2}) these are
635 typically weak on most days, and indeed the mean over the entire period already gives a robust estimate of the true
636 parameter value (Fig. 13). The parameters with the strongest correlations are R_{CO} of households and road traffic,
637 and their mean values tend to be dominated by a few outliers. Selecting days on which the posterior parameter
638 correlations are weak (i.e. the atmospheric signal clearly contains information about this specific parameter) results
639 in a large improvement compared to the prior or a 14-day average. Moreover, these results show a similar or better
640 performance as the top-3 selection based on Fig. 12 (0.08 for EF3 and 0.18 for R_{co} 7A, not shown), and are closer
641 to the base run.

642

643 **Figure 13. Scatter plot of the absolute error in the scaling factor of the industrial emission factor (EF 3) and R_{CO} of road**
644 **traffic (7A) against the sum of the parameter correlations of the same parameters. The correlation coefficients are -0.17**
645 **and 0.37 respectively. The horizontal lines give the average absolute error in the scaling factor for the prior (full black**
646 **line), if all 14 days are averaged (dotted line), and based on the 3 days with the smallest parameter correlations (dashed**
647 **line) and the result for the base run (full red line). The values are also given.**

648 **4 Discussion**

649 **4.1 Optimizing the dynamic emission model**

650 The dynamic emission model has the advantage over static emission fields that its parameters are optimized, giving
651 physical meaning to the results. To reduce the size of the problem, the state vector can be populated with those
652 parameters that are most important and/or uncertain. However, we find that uncertain, non-included parameters
653 can still significantly affect the optimization. Therefore, the size of the state vector should be considered carefully
654 when applying this method. Moreover, we performed an experiment to establish the possibility to optimize the
655 time profiles as part of the state vector. Although we found some improvements, it appears to be difficult to
656 differentiate between the different variables in Eq. (2) that have a linear relationship based purely on the

657 observations. Therefore, the results are not shown and optimizing the temporal dynamics of the emission model

658 requires further work.

659 Additionally, we identified the base run as the simplest method to get good estimates, but we do note that our

660 current propagation scheme does not yet include error growth. That means that eventually the ensemble will

661 converge on a parameter value and discard incoming observational evidence, unless the covariance is inflated to

662 allow new updates. Examples of such a covariance inflation scheme are ample in literature and in principle not

663 difficult to include, but were not yet considered in this work as the time periods covered were still short.

664 Finally, we have demonstrated that tracers are suitable for source attribution. Several previous studies have used

665 co-emitted species as tracer for fossil fuel CO_2 by taking advantage of the specific emission ratio characteristics

666 of each source sector (Lauvaux et al., 2013; Lindenmaier et al., 2014; Turnbull et al., 2015) and came to similar

667 conclusions. Nevertheless, the uncertainty in emission ratios remains a source of error and therefore the

668 optimization of emission ratios with our system is a promising step forward. Using co-emitted species to identify

669 the total fossil fuel contribution to the observed CO_2 signal is more difficult (Turnbull et al., 2006). The reason for

670 this is that there is a large variability in emission ratios between sectors. This makes it difficult to establish an

671 average emission ratio for an urban area, because it depends strongly on the relative contribution of each source

672 sector and may vary over time.

4.2 Radiocarbon and background definition

674 Therefore, a nice addition to this inversion system would be the inclusion of radiocarbon measurements. The

675 radiocarbon isotope ($^{14}CO_2$) can be used to simulate fossil fuel CO_2 records and has been applied successfully in

676 several inverse modelling studies (Turnbull et al., 2006; Levin and Karstens, 2007; Miller et al., 2012; Turnbull et

677 al., 2015; Basu et al., 2016; Wang et al., 2018). The radiocarbon measurements could be used directly in the

678 inversion (as we did with the co-emitted species) or be used to define a fossil fuel CO_2 record in advance (Fischer

679 et al., 2017; Graven et al., 2018). Our urban network detects average fossil fuel CO_2 signals of about 5 ppm with

680 peaks up to 50 ppm. This would result in $\Delta^{14}C$ signals (the ratio of $^{14}CO_2$ to $^{12}CO_2$) of around 13 up to 130 per

681 mille, which are certainly detectable with current techniques. However, observations of carbon isotopes are

682 expensive and currently not widely available, so their applicability is still limited. Besides $\Delta^{14}C$ other isotope

683 signatures and tracers can also provide additional information. For example, $^{13}CO_2$ and O_2/N_2 can give insight in

684 the dominant sources and sinks or fuel types (Lopez et al., 2013; Van der Laan et al., 2014) and as such be an

685 indicator for the transition from fossil fuels to biofuels. They might also help to separate between the stack

686 emissions of industry and coal- and gas-fired power plants.

687 An additional advantage of including the radiocarbon isotope is that the uncertainty in the background CO_2 can be

688 excluded, i.e. only the fossil fuel record is considered. Here, we choose to ignore the uncertainty in the background,

689 except in the definition of the covariance matrix R, and attribute all tracer residuals to the fossil fuel emissions.

690 Yet an incorrect definition of the background causes a large bias in the optimized emissions (Göckede et al., 2010).

691 There are also several other methods to deal with the non-fossil fuel related CO_2 signals. First, the uncertain

692 background can be added to the state vector and be optimized in the inversion. For example, He et al. (2018) have

693 shown that high-altitude aircraft observations are suitable to improve regional biosphere flux estimates by

694 correcting the bias in boundary conditions. Second, a mole fraction gradient over the area of interest can be

695 calculated using an upwind and downwind site such that the boundary inflow plays no role anymore (Turnbull et

696 al., 2015). This method was shown to reduce the impact of boundary inflow, but only when the wind direction is

697 more or less perpendicular to the gradient (Bréon et al., 2015; Staufer et al., 2016). Therefore, this method limits

698 the amount of useful measurements.

4.3 Error correlations

700 The dynamic emission model also allows us to study the correlations between model parameters, therefore giving

701 more insight in how information can be used in the system and which parameters are more challenging to separate.

702 Previously, Boschetti et al. (2018) have used the presence of error correlations between emissions of different

703 species and found that this reduces the posterior uncertainties for all species. They even show that the uncertainty

704 reduction increases with the correlation and that an incorrect definition of the error correlations may cause a

705 systematic bias in the posterior emission estimate. However, error correlations are only beneficial if the

706 atmospheric observations can distinguish between the correlated parameters. If this is not the case the presence of

707 parameter correlations can result in poorly constrained parameters and/or large posterior uncertainties. This is

708 especially true when parameters are sensitive to parameter correlations, as we show for R_{CO} of road traffic.

709 An important question is then why some emission model parameters are more sensitive to the presence of

710 parameter correlations than others. One hypothesis is that parameters with a lower prior uncertainty are more

711 sensitive to the presence of parameter correlations. The idea behind this is that if we reduce the diagonal value

712 (uncertainty) by a factor of 4 the off-diagonal value (parameter correlation) reduces by a factor of 2. This means

713 that the parameter correlation is relatively stronger if the uncertainty is lower (Boschetti et al., 2018). This

714 hypothesis cannot be confirmed by our results, as we only find a correlation of -0.27 between the prior uncertainty

715 and the sensitivity to parameter correlations (defined as the correlation between the posterior uncertainty and the

716 sum of the parameter correlations). The main difficulty here is that not all parameters can be discerned with the

717 observed atmospheric signals. Although we included the additional co-emitted tracers for source attribution, the

718 emission ratios have a large uncertainty and the system can have difficulties assigning residuals to either the

719 emission ratio or the emission factor. Yet if we calculate an average sensitivity and total posterior uncertainty per

720 sector (by combining the emission factor and emission ratios per sector) we find a correlation coefficient of -0.82.

721 This suggests that this hypothesis might indeed be correct and source sectors with larger parameter uncertainties

722 are less sensitive to the presence of parameter correlations.

4.4 Atmospheric transport model errors

724 In addition to the experiments described in Sect. 2.3 we conducted an experiment that focused on the role of

725 transport model errors by using observed meteorology to drive the OPS model in the inversion. Like many authors

726 before us (McKain et al., 2012; Brioude et al., 2013; Lauvaux et al., 2013; Bréon et al., 2015; Boon et al., 2016)

727 we found a large impact on the performance of our system and once again confirmed the need for accurate transport

728 models. This experiment is not further shown in this work because of its redundancy with previous conclusions.

729 Nevertheless, we performed this experiment to examine whether transport errors are important when the state

730 vector consists of parameters that are valid for the entire domain. Random errors, such as errors in the wind

731 direction, are unlikely to affect the optimized emissions much when averaged over a longer time period and

732 domain. This was shown by Deng et al. (2017), who found little variation in the average CO_2 emission for

733 Indianapolis using different configurations of WRF to calculate the transport. However, they did find an impact

734   on the spatial distribution of the emissions. This becomes important when optimizing a specific source sector that

735   is clustered in one place, such as the glasshouses. We found that the glasshouse sector is only correctly optimized

736   with a specific wind direction. If the modelled wind direction is wrong the residuals would thus not be attributed

737   to the glasshouse sector as it is not in the modelled footprint of the measurement site. As such, we conclude that

738   the footprint definition has an impact on the optimized parameters, despite that the parameters have no spatial

739   distribution. Similarly, Broquet et al. (2018) mention that the location and structure of a simulated urban plume

740   might differ significantly from the true plume characteristics due to errors in the simulated wind speed and wind

741   direction.

742   Systematic errors, whether in the modelled transport or in the observations, are more difficult to solve as they do

743   not cancel out when simulating a longer period, and this can lead to biased emission estimates (Meirink et al.,

744   2008; Su et al., 2011). Several methods have been suggested to overcome problems with an incorrect description

745   of atmospheric transport, such as using an ensemble of atmospheric transport model simulations (Angevine et al.,

746   2014) or the assimilation of meteorological observations (Lauvaux et al., 2013). The latter showed lower biases in

747   buoyancy and mean horizontal wind speed. Another method that is often used is the selection of well-mixed

748   afternoon hours to exclude stable conditions under which pollutant dispersion is often poorly represented (Lauvaux

749   et al., 2013; Bréon et al., 2015; Boon et al., 2016). Such data selection however leads to a bias in the estimated

750   emissions when the diurnal cycle is not correctly accounted for (Super et al., 2019).

751   Here, we also applied a daytime selection criterion to mimic this situation. However, we found that night time

752   hours could be very useful to constrain our emissions. In our DA system we use residual fossil fuel enhancements

753   over a background (prior - true mole fraction enhancement) to constrain the fossil fuel fluxes. The larger the

754   residual, the more information can be gained from it since the impact of the observation error (R matrix) is

755   relatively small. If, for example, the industrial emission factor is underestimated by 10 %, the residual industrial

756   enhancement (given a linear relationship between the emission factor and the total emission from this sector) will

757   be 10 % of the pseudo-observed mole fraction. This means that a large signal from the industry is needed to reach

758   a residual that is larger than the observation error (σ is 1.6 ppm for CO_2). Looking at the time series of pseudo-

759   observations we find that such large signals mostly occur during night time or in the early morning. Therefore, the

760   inversion could benefit strongly from an improved description of night time boundary layers and stable conditions,

761   so that the large night time enhancements can be used to constrain the fossil fuel fluxes.

762   **5 Conclusions**

763   The aim of this study was to examine how well our DA system can quantify urban CO_2 emissions per source

764   sector. Since the prior consists of a dynamic fossil fuel emission model the model parameters are optimized rather

765   than the emissions themselves. The parameters are related to specific source sectors and to attribute residuals to

766   these sectors measurements of additional tracers (CO, NO_x and SO_2) are included in the inversions. We tested this

767   system to examine its ability to overcome some major limitations in current urban-scale inversions: source

768   attribution, definition of the prior and its uncertainties, and the sensitivity to errors in atmospheric transport.

769   We find that inverse modelling at the urban scale is feasible when the observations contain a lot of information

770   about the different source sectors. When only CO_2 mole fractions are used in the inversion the total CO_2 emission

771   are well-constrained. Additional tracers are an important addition to the inversion framework in order to discern

772   the information belonging to specific source sectors and emission model parameters. However, even more tracers

773 might be needed to fully capture the heterogeneity of the emission landscape. Moreover, we argue that a dynamic

774 emission model has some major advantages over regular emission maps, allowing us to constrain physically

775 relevant parameters even in the absence of good prior information.

776 Nevertheless, quite some challenges remain. Transport modelling at this small scale needs to be improved to be

777 able to use real urban observations, as under current conditions the transport error strongly dominates the results.

778 Especially improving the description of night time boundary layers could be beneficial, because large atmospheric

779 signals mostly occur during the period. For the future, additional advances need to be made to include satellite

780 observations in the inverse modelling framework. The advantage of satellite data is that it covers data-sparse

781 regions and with a larger view it can differentiate between the urban dome with high pollution levels and the

782 cleaner rural areas, which is a nice addition to in situ measurements.

783 **Code and data availability**

784 The availability of the CTDAS (v1.0) code is described in a previous publication (Van der Laan-Luijkx et al.,

785 2017), which forms the basis of the system described in this paper. Minor changes have been made to include the

786 dynamic emission model. Revised code and the additional module used to describe the dynamic emission model

787 and the creation of pseudo-observations is included as Supplement, as is a script used for the emission uncertainty

788 analysis (Monte Carlo simulation). Input data for the dynamic emission model are taken from open, online

789 databases and are summarized in Appendix A, including their data sources. Example input files for CTDAS and

790 the OPS model are also included as Supplement.

Geoscientific
Model Development
Discussions

791 **Appendix A**

792 **Table A1. Overview of all parameters in the dynamic emission model, their unit, function type, expected value and**
793 **uncertainty (range).**

Parameter	(Sub)sector	Unit	Function type	Expected value	Uncertainty
Emission factor[a]	Coal-fired power plants[c]	kg PJ^{-1}	Normal	1.01E8	23 %
	Gas-fired power plants[c]	kg PJ^{-1}	normal	5.61E7	10 %
	Households[c]	kg PJ^{-1}	normal	5.89E7	14 %
	Glasshouses[c]	kg PJ^{-1}	normal	5.61E7	25 %
	Industry[d]	kg PJ^{-1}	normal	7.66E7	40 %
	Road traffic cars[e]	kg PJ^{-1}	normal	7.24E7	10 %
	Road traffic HDV[e]	kg PJ^{-1}	normal	7.33E7	5 %
	Ocean shipping[f]	kg PJ^{-1}	normal	7.76E7	5 %
	Inland shipping[f]	kg PJ^{-1}	normal	7.30E7	5 %
	Recreational shipping[f]	kg PJ^{-1}	normal	7.10E7	5 %
Emission ratio CO:CO$_2$	Coal-fired power plants[e]	kg kg^{-1}	lognormal	1.29E-4	8.7E-7–2.9E-4
	Gas-fired power plants[e]	kg kg^{-1}	lognormal	8.47E-4	3.4E-4–2.5E-3
	Households[e]	kg kg^{-1}	lognormal	3.88E-3	8.3E-4–9.6E-3
	Glasshouses[e]	kg kg^{-1}	lognormal	5.40E-4	3.1E-5–7.7E-4
	Industry[d]	kg kg^{-1}	normal	2.06E-3	40 %
	Road traffic cars[e]	kg kg^{-1}	lognormal	1.32E-2	8.0E-5–6.5E-2
	Road traffic HDV[e]	kg kg^{-1}	lognormal	2.22E-3	9.3E-5–1.3E-2
	Ocean shipping[f]	kg kg^{-1}	normal	2.32E-3	30 %
	Inland shipping[f]	kg kg^{-1}	normal	3.42E-3	30 %
	Recreational shipping[f]	kg kg^{-1}	normal	2.96E-1	30 %
Emission ratio NO$_x$:CO$_2$	Coal-fired power plants[e]	kg kg^{-1}	lognormal	5.94E-4	3.0E-4–9.4E-4
	Gas-fired power plants[e]	kg kg^{-1}	lognormal	2.00E-3	2.6E-4–3.7E-3
	Households[e]	kg kg^{-1}	lognormal	1.50E-3	4.8E-4–3.3E-3
	Glasshouses[e]	kg kg^{-1}	lognormal	1.63E-3	5.0E-4–3.5E-3
	Industry[d]	kg kg^{-1}	normal	6.56E-4	40 %
	Road traffic cars[e]	kg kg^{-1}	lognormal	1.76E-3	9.0E-5–7.5E-3
	Road traffic HDV[e]	kg kg^{-1}	lognormal	1.11E-2	3.3E-4–3.7E-2

	Ocean shipping[f]	kg kg^{-1}	normal	2.32E-2	30 %
	Inland shipping[f]	kg kg^{-1}	normal	1.37E-2	30 %
	Recreational shipping[f]	kg kg^{-1}	normal	1.97E-3	30 %
Emission ratio SO$_2$:CO$_2$	Coal-fired power plants[e]	kg kg^{-1}	lognormal	1.66E-4	2.9E-5–4.4E-4
	Gas-fired power plants[e]	kg kg^{-1}	lognormal	5.01E-6	2.9E-6–7.2E-6
	Households[e]	kg kg^{-1}	lognormal	2.21E-5	1.4E-5–6.7E-5
	Glasshouses[e]	kg kg^{-1}	lognormal	8.91E-6	5.2E-6–1.3E-5
	Industry[d]	kg kg^{-1}	normal	4.28E-4	40 %
	Road traffic cars[g]	kg kg^{-1}	normal	1.01E-6	100 %
	Road traffic HDV[g]	kg kg^{-1}	normal	8.16E-7	100 %
	Ocean shipping[f]	kg kg^{-1}	lognormal	6.18E-3	3.3E-4–2.0E-2
	Inland shipping[f]	kg kg^{-1}	lognormal	6.57E-3	3.5E-4–3.0E-2
	Recreational shipping[f]	kg kg^{-1}	lognormal	3.14E-4	1.1E-4–7.0E-4
Hourly time factor[h]	Coal-fired power plants	-	normal	1	28 %
	Gas-fired power plants	-	normal	1	43 %
	Industry	-	normal	1	5 %
	Households	-	normal	1	43 %
	Glasshouses	-	normal	1	74 %
	Road traffic cars highway	-	normal	1	18 %
	Road traffic cars main road	-	normal	1	18 %
	Road traffic cars urban road	-	normal	1	18 %
	Road traffic HDV highway	-	normal	1	41 %
	Road traffic HDV main road	-	normal	1	18 %
	Road traffic HDV urban road	-	normal	1	48 %
	Total shipping	-	normal	1	31 %
Energy consumption per activity data[i]	Total power plants	PJ/mln €	-	8.22E-4	-
	Households	PJ/dd[b]	-	0.199	-
	Glasshouses	PJ/dd[b]	-	0.061	-
	Industry	PJ/mln €	-	7.05E-4	-
	Road traffic cars	PJ/mln €	-	3.98E-4	-

Geoscientific
Model Development
Discussions

EGU

	Road traffic HDV	PJ/mln €	-	2.01E-4	-
	Total shipping	PJ/mln €	-	1.51E-4	-
Fraction of total energy consumption per subsector[j]	Total power plants: coal	-	-	0.62	-
	Total power plants: gas	-	-	0.38	-
	Road traffic cars: highway	-	-	0.47	-
	Road traffic cars: main road	-	-	0.28	-
	Road traffic cars: urban road	-	-	0.25	-
	Road traffic HDV: highway	-	-	0.56	-
	Road traffic HDV: main road	-	-	0.24	-
	Road traffic HDV: urban road	-	-	0.20	-
	Total shipping: ocean	-	-	0.79	-
	Total shipping: inland	-	-	0.20	-
	Total shipping: recreational	-	-	0.01	-

794 [a] Emission factor for coal-fired and gas-fired power plants include uncertainty due to variations in fuel type, including burning

795 of biomass (5 % uncertainty). For households assume 8 % wood combustion based on CO_2 emission values (*Vernieuwd*

796 *emissiemodel houtkachels*, by B.I. Jansen (TNO, 2016)), the remainder is natural gas (with 10 % uncertainty). For glasshouses

797 assume only natural gas combustion, including 20 % additional uncertainty due to use of cogeneration plants. For road traffic

798 cars assume 69 % gasoline, 29 % diesel and 2 % LPG (with 5 % uncertainty); for road traffic HDV assume 100 % diesel.

799 [b] dd = degree day

800 [c] Expected value and uncertainty based on IPCC Emission Factor Database (EFDB) using 2006 IPCC guidelines

801 [d] Expected value based on Emissieregistratie (emission) and CBS (energy consumption); uncertainty based on expert

802 judgement

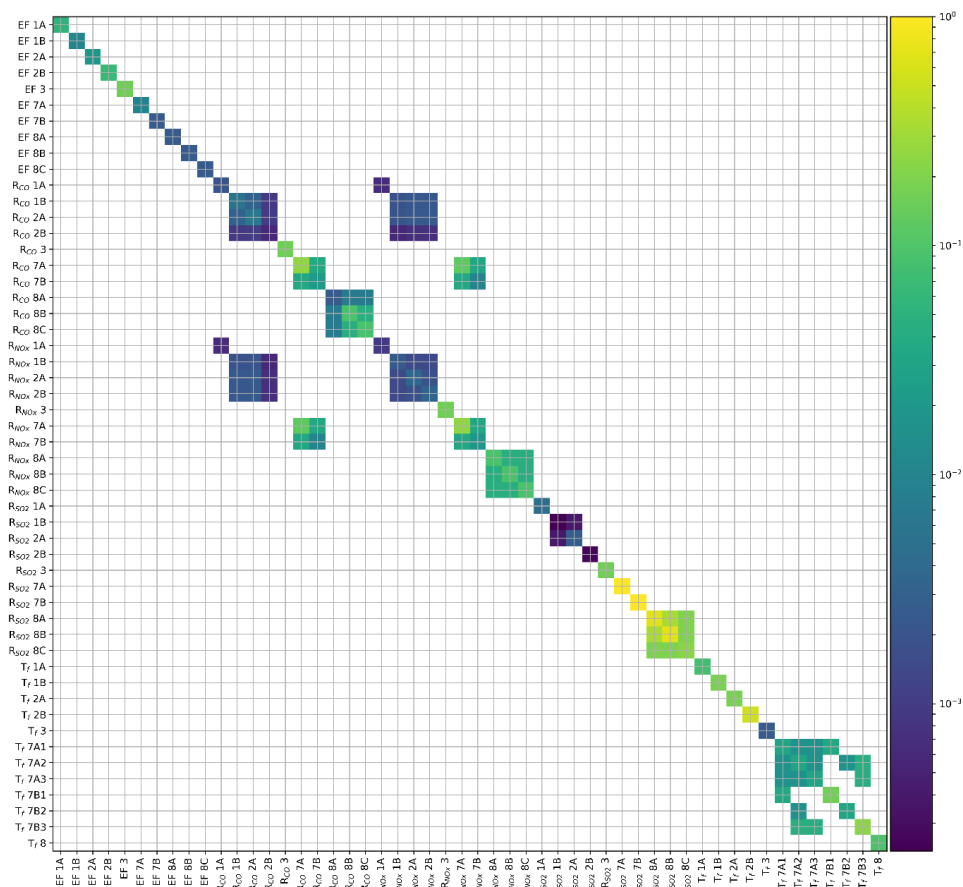803 [e] Expected value and uncertainty based on the EMEP/EEA air pollutant emission inventory guidebook 2016

804 [f] Expected value and uncertainty based on *CO₂, CH₄, and N₂O emissions from transportation-water-borne navigation*, by Paul

805 Jun, Michael Gillenwater, and Wiley Barbour (Good Practice Guidance and Uncertainty Management in National Greenhouse

806 Gas Inventories)

807 [g] Expected value based on Air Pollutant Emission Factor Library (Finish Environment Institute); uncertainty based on expert

808 judgement

809 [h] Uncertainties based on comparison activity data-based time profiles and estimated time profiles from environmental/socio-

810 economic factors

811 [i] Expected value based on CBS (energy consumption, GDP) and KNMI (degree day sum)
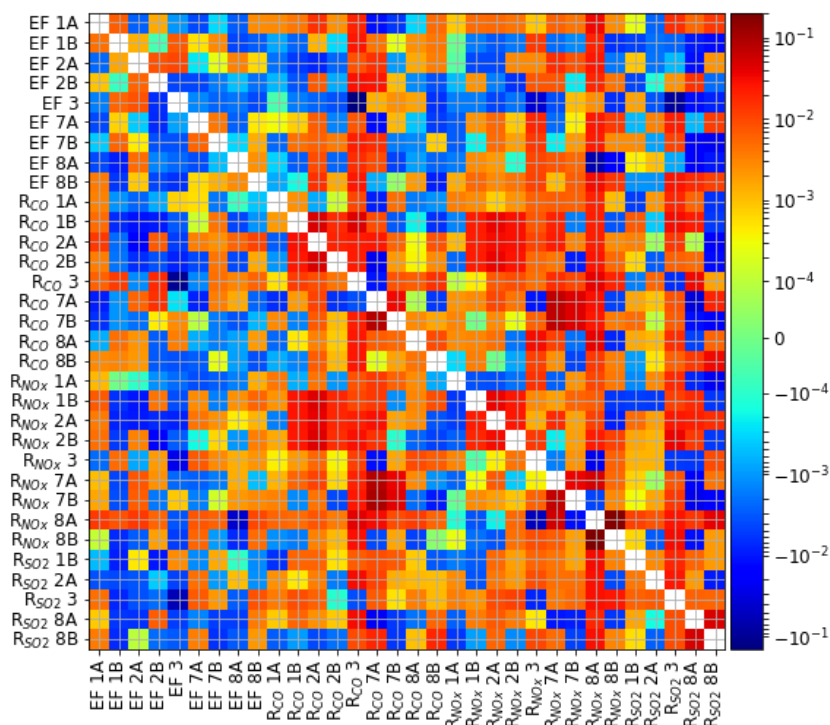
812 [j] Expected value based on Emissieregistratie

Figure A1. Covariance matrix for all parameters in the dynamic emission model. For all covariances we assume a correlation coefficient of 0.5. (Sub)sectors are indicated with their short names as summarized in Table 1. Note that the time profiles of road traffic emissions are specified per road type (1 = highway, 2 = main road, 3 = urban road).

Appendix B

Figure B1. Matrix showing the difference in correlation coefficient (r) between the CO$_2$_only_no_propagation and No_propagation run averaged for all 14 days, where positive differences indicate reduced parameter correlations when all tracers are included (No_propagation). (Sub)sectors are indicated with their short names as summarized in Table 1. For some parameters a strong reduction in parameter correlations is shown, indicating that with all tracers that parameter can be more easily separated from others, for example the emission factors of industry and coal-fired power plants (EF3 and EF1B).

Author contribution

The initial ideas are developed by WP, IS, HACDvdG and MKvdM. IS and SNCD developed the dynamic emission model. IS and WP are responsible for setting up the inverse modelling experiments and prepared the manuscript with contributions from all co-authors.

Competing interests

The authors declare that they have no conflict of interest.

Acknowledgments

834 CITY (APIN0029 2015-3.1-029 P040-04) and the EIT Climate-KIC Fellows programme (ARED0004 2013-1.1-

835 008 P017-0x).

836 **References**

837 Andres, R. J., Boden, T. A., and Higdon, D.: A new evaluation of the uncertainty associated with CDIAC estimates

838 of fossil fuel carbon dioxide emission, Tellus B Chem. Phys. Meteorol., 66, 23616, 10.3402/tellusb.v66.23616,

839 2014.

840 Andres, R. J., Boden, T. A., and Higdon, D. M.: Gridded uncertainty in fossil fuel carbon dioxide emission maps,

841 a CDIAC example, Atmos. Chem. Phys., 16, 14979-14995, 10.5194/acp-16-14979-2016, 2016.

842 Angevine, W. M., Brioude, J., McKeen, S., and Holloway, J. S.: Uncertainty in Lagrangian pollutant transport

843 simulations due to meteorological uncertainty from a mesoscale WRF ensemble, Geosci. Model Dev., 7, 2817-

844 2829, 10.5194/gmd-7-2817-2014, 2014.

845 Asefi-Najafabady, S., Rayner, P. J., Gurney, K. R., McRobert, A., Song, Y., Coltin, K., Huang, J., Elvidge, C.,

846 and Baugh, K.: A multiyear, global gridded fossil fuel CO_2 emission data product: Evaluation and analysis of

847 results, J. Geophys. Res.-Atmos., 119, 10,213-210,231, 10.1002/2013jd021296, 2014.

848 Basu, S., Miller, J. B., and Lehman, S.: Separation of biospheric and fossil fuel fluxes of CO_2 by atmospheric

849 inversion of CO_2 and $^{14}CO_2$ measurements: Observation System Simulations, Atmos. Chem. Phys., 16, 5665-5683,

850 10.5194/acp-16-5665-2016, 2016.

851 Boon, A., Broquet, G., Clifford, D. J., Chevallier, F., Butterfield, D. M., Pison, I., Ramonet, M., Paris, J. D., and

852 Ciais, P.: Analysis of the potential of near-ground measurements of CO_2 and CH_4 in London, UK, for the

853 monitoring of city-scale emissions using an atmospheric transport model, Atmos. Chem. Phys., 16, 6735-6756,

854 10.5194/acp-16-6735-2016, 2016.

855 Boschetti, F., Thouret, V., Maenhout, G. J., Totsche, K. U., Marshall, J., and Gerbig, C.: Multi-species inversion

856 and IAGOS airborne data for a better constraint of continental-scale fluxes, Atmos. Chem. Phys., 18, 9225-9241,

857 10.5194/acp-18-9225-2018, 2018.

858 Bréon, F. M., Broquet, G., Puygrenier, V., Chevallier, F., Xueref-Remy, I., Ramonet, M., Dieudonné, E., Lopez,

859 M., Schmidt, M., Perrussel, O., and Ciais, P.: An attempt at estimating Paris area CO_2 emissions from atmospheric

860 concentration measurements, Atmos. Chem. Phys., 15, 1707-1724, 10.5194/acp-15-1707-2015, 2015.

861 Brioude, J., Angevine, W. M., Ahmadov, R., Kim, S. W., Evan, S., McKeen, S. A., Hsie, E. Y., Frost, G. J.,

862 Neuman, J. A., Pollack, I. B., Peischl, J., Ryerson, T. B., Holloway, J., Brown, S. S., Nowak, J. B., Roberts, J. M.,

863 Wofsy, S. C., Santoni, G. W., Oda, T., and Trainer, M.: Top-down estimate of surface flux in the Los Angeles

864 Basin using a mesoscale inverse modeling technique: Assessing anthropogenic emissions of CO, NO_x and CO_2

865 and their impacts, Atmos. Chem. Phys., 13, 3661-3677, 10.5194/acp-13-3661-2013, 2013.

866 Brophy, K., Graven, H., Manning, A. J., White, E., Arnold, T., Fischer, M. L., Jeong, S., Cui, X., and Rigby, M.:

867 Characterizing uncertainties in atmospheric inversions of fossil fuel CO_2 emissions in California, Atmos. Chem.

868 Phys. Discuss., 2018, 1-44, 10.5194/acp-2018-473, 2018.

869 Broquet, G., Bréon, F. M., Renault, E., Buchwitz, M., Reuter, M., Bovensmann, H., Chevallier, F., Wu, L., and

870 Ciais, P.: The potential of satellite spectro-imagery for monitoring CO_2 emissions from large cities, Atmos. Meas.

871 Tech., 11, 681-708, 10.5194/amt-11-681-2018, 2018.

33

872   Chevallier, F., Viovy, N., Reichstein, M., and Ciais, P.: On the assignment of prior errors in Bayesian inversions
873   of CO2 surface fluxes, Geophys. Res. Lett., 33, doi:10.1029/2006GL026496, 2006.
874   Ciais, P., Paris, J. D., Marland, G., Peylin, P., Piao, S. L., Levin, I., Pregger, T., Scholz, Y., Friedrich, R., Rivier,
875   L., Houwelling, S., and Schulze, E. D.: The European carbon balance. Part 1: Fossil fuel emissions, Glob. Change
876   Biol., 16, 1395-1408, 10.1111/j.1365-2486.2009.02098.x, 2010.
877   Deng, A., Lauvaux, T., Davis, K. J., Gaudet, B. J., Miles, N., Richardson, S. J., Wu, K., Sarmiento, D. P., Hardesty,
878   R. M., Bonin, T. A., Brewer, W. A., and Gurney, K. R.: Toward reduced transport errors in a high resolution urban
879   CO$_2$ inversion system, Elementa (Wash. D.C.), 5, 10.1525/elementa.133, 2017.
880   Denier van der Gon, H. A. C., Hendriks, C., Kuenen, J., Segers, A., and Visschedijk, A.: Description of current
881   temporal emission patterns and sensitivity of predicted AQ for temporal emission patterns, TNO, Utrecht, 2011.
882   Djuricin, S., Pataki, D. E., and Xu, X.: A comparison of tracer methods for quantifying CO$_2$ sources in an urban
883   region, J. Geophys. Res.-Atmos., 115, 1-13, 10.1029/2009JD012236, 2010.
884   Fauser, P., Sørensen, P. B., Nielsen, M., Winther, M., Plejdrup, M. S., Hoffmann, L., Gyldenkærne, S., Mikkelsen,
885   M. H., Albrektsen, R., Lyck, E., Thomsen, M., Hjelgaard, K., and Nielsen, O.-K.: Monte Carlo (Tier 2) uncertainty
886   analysis of Danish Greenhouse gas emission inventory, Greenhouse Gas Measurement and Management, 1, 145-
887   160, 10.1080/20430779.2011.621949, 2011.
888   Fischer, M. L., Parazoo, N., Brophy, K., Cui, X., Jeong, S., Liu, J., Keeling, R., Taylor, T. E., Gurney, K., Oda,
889   T., and Graven, H.: Simulating estimation of California fossil fuel and biosphere carbon dioxide exchanges
890   combining in situ tower and satellite column observations, J. Geophys. Res.-Atmos., 122, 3653-3671,
891   10.1002/2016jd025617, 2017.
892   Gerbig, C., Lin, J. C., Wofsy, S. C., Daube, B. C., Andrews, A. E., Stephens, B. B., Bakwin, P. S., and Grainger,
893   C. A.: Toward constraining regional-scale fluxes of CO$_2$ with atmospheric observations over a continent: 2.
894   Analysis of COBRA data using a receptor-oriented framework, J. Geophys. Res.-Atmos., 108,
895   10.1029/2003JD003770, 2003.
896   Göckede, M., Turner, D. P., Michalak, A. M., Vickers, D., and Law, B. E.: Sensitivity of a subregional scale
897   atmospheric inverse CO$_2$ modeling framework to boundary conditions, J. Geophys. Res.-Atmos., 115,
898   10.1029/2010JD014443, 2010.
899   Graven, H., Fischer, M. L., Lueker, T., Jeong, S., Guilderson, T. P., Keeling, R. F., Bambha, R., Brophy, K.,
900   Callahan, W., Cui, X., Frankenberg, C., Gurney, K. R., LaFranchi, B. W., Lehman, S. J., Michelsen, H., Miller, J.
901   B., Newman, S., Paplawsky, W., Parazoo, N. C., Sloop, C., and Walker, S. J.: Assessing fossil fuel CO$_2$ emissions
902   in California using atmospheric observations and models, Environ. Res. Lett., 13, 065007, 10.1088/1748-
903   9326/aabd43, 2018.
904   Gurney, K. R., Patarasuk, R., Liang, J., Song, Y., O'Keeffe, D., Rao, P., Whetstone, J. R., Duren, R. M., Eldering,
905   A., and Miller, C.: The Hestia fossil fuel CO2 emissions data product for the Los Angeles Megacity (Hestia-LA),
906   Earth Syst. Sci. Data Discuss., 2019, 1-38, 10.5194/essd-2018-162, 2019.
907   He, W., Van der Velde, I. R., Andrews, A. E., Sweeney, C., Miller, J., Tans, P., Van der Laan-Luijkx, I. T.,
908   Nehrkorn, T., Mountain, M., Ju, W., Peters, W., and Chen, H.: CTDAS-Lagrange v1.0: a high-resolution data
909   assimilation system for regional carbon dioxide observations, Geosci. Model Dev., 11, 3515-3536, 10.5194/gmd-
910   11-3515-2018, 2018.

34

911   Hogue, S., Marland, E., Andres, R. J., Marland, G., and Woodard, D.: Uncertainty in gridded CO2 emissions

912   estimates, Earth's Future, 4, 225-239, doi:10.1002/2015EF000343, 2016.

913   Huijnen, V., Williams, J., van Weele, M., van Noije, T., Krol, M., Dentener, F., Segers, A., Houweling, S., Peters,

914   W., de Laat, J., Boersma, F., Bergamaschi, P., van Velthoven, P., Le Sager, P., Eskes, H., Alkemade, F., Scheele,

915   R., Nédélec, P., and Pätz, H. W.: The global chemistry transport model TM5: description and evaluation of the

916   tropospheric chemistry version 3.0, Geosci. Model Dev., 3, 445-473, 10.5194/gmd-3-445-2010, 2010.

917   Hutchins, M. G., Colby, J. D., Marland, G., and Marland, E.: A comparison of five high-resolution spatially-

918   explicit, fossil-fuel, carbon dioxide emission inventories for the United States, Mitig. Adapt. Strat. Gl., 22, 947-

919   972, 10.1007/s11027-016-9709-9, 2017.

920   IEA: World Energy Outlook 2008, International Energy Agency, Paris, 2008.

921   Kuenen, J. J. P., Visschedijk, A. J. H., Jozwicka, M., and Denier van der Gon, H. A. C.: TNO-MACC-II emission

922   inventory; A multi-year (2003-2009) consistent high-resolution European emission inventory for air quality

923   modelling, Atmos. Chem. Phys., 14, 10963-10976, 10.5194/acp-14-10963-2014, 2014.

924   LaFranchi, B. W., Pétron, G., Miller, J. B., Lehman, S. J., Andrews, A. E., Dlugokencky, E. J., Hall, B., Miller, B.

925   R., Montzka, S. A., Neff, W., Novelli, P. C., Sweeney, C., Turnbull, J. C., Wolfe, D. E., Tans, P. P., Gurney, K.

926   R., and Guilderson, T. P.: Constraints on emissions of carbon monoxide, methane, and a suite of hydrocarbons in

927   the Colorado front range using observations of $^{14}CO_2$, Atmos. Chem. Phys., 13, 11101-11120, 10.5194/acp-13-

928   11101-2013, 2013.

929   Lauvaux, T., Miles, N. L., Richardson, S. J., Deng, A., Stauffer, D. R., Davis, K. J., Jacobson, G., Rella, C.,

930   Calonder, G. P., and Decola, P. L.: Urban emissions of CO_2 from Davos, Switzerland: The first real-time

931   monitoring system using an atmospheric inversion technique, J. Appl. Meteorol. Clim., 52, 2654-2668,

932   10.1175/JAMC-D-13-038.1, 2013.

933   Lauvaux, T., Miles, N. L., Deng, A., Richardson, S. J., Cambaliza, M. O., Davis, K. J., Gaudet, B., Gurney, K. R.,

934   Huang, J., O'Keefe, D., Song, Y., Karion, A., Oda, T., Patarasuk, R., Razlivanov, I., Sarmiento, D., Shepson, P.,

935   Sweeney, C., Turnbull, J., and Wu, K.: High-resolution atmospheric inversion of urban CO_2 emissions during the

936   dormant season of the Indianapolis Flux Experiment (INFLUX), J. Geophys. Res.-Atmos., 121, 5213-5236,

937   10.1002/2015jd024473, 2016.

938   Levin, I., and Karstens, U.: Inferring high-resolution fossil fuel CO_2 records at continental sites from combined

939    $^{14}CO_2$ and CO observations, Tellus B Chem. Phys. Meteorol., 59, 245-250, 10.1111/j.1600-0889.2006.00244.x,

940   2007.

941   Liander: Innovatie & Diensten: Open data: https://www.liander.nl/over-liander/innovatie/open-data/data, last

942   access: Feb 2018.

943   Lin, J. C., Gerbig, C., Wofsy, S. C., Andrews, A. E., Daube, B. C., Davis, K. J., and Grainger, C. A. C.: A near-

944   field tool for simulating the upstream influence of atmospheric observations: The Stochastic Time-Inverted

945   Lagrangian Transport (STILT) model, J. Geophys. Res.-Atmos., 108, 10.1029/2002jd003161, 2003.

946   Lindenmaier, R., Dubey, M. K., Henderson, B. G., Butterfield, Z. T., Herman, J. R., Rahn, T., and Lee, S. H.:

947   Multiscale observations of CO_2, $^{13}CO_2$, and pollutants at Four Corners for emission verification and attribution,

948   in: P. Natl. Acad. Sci. USA, 2014, 8386-8391, 2014.

949   Lopez, M., Schmidt, M., Delmotte, M., Colomb, A., Gros, V., Janssen, C., Lehman, S. J., Mondelain, D., Perrussel,

950   O., Ramonet, M., Xueref-Remy, I., and Bousquet, P.: CO, NO_x and $^{13}CO_2$ as tracers for fossil fuel CO_2: Results

Geoscientific
Model Development
Discussions

951 from a pilot study in Paris during winter 2010, Atmos. Chem. Phys., 13, 7343-7358, 10.5194/acp-13-7343-2013,
952 2013.

953 McKain, K., Wofsy, S. C., Nehrkorn, T., Eluszkiewicz, J., Ehleringer, J. R., and Stephens, B. B.: Assessment of
954 ground-based atmospheric observations for verification of greenhouse gas emissions from an urban region, in: P.
955 Natl. Acad. Sci. USA, 2012, 8423-8428, 2012.

956 Meirink, J. F., Bergamaschi, P., Frankenberg, C., d'Amelio, M. T. S., Dlugokencky, E. J., Gatti, L. V., Houweling,
957 S., Miller, J. B., Röckmann, T., Villani, M. G., and Krol, M. C.: Four-dimensional variational data assimilation
958 for inverse modeling of atmospheric methane emissions: Analysis of SCIAMACHY observations, J. Geophys.
959 Res.-Atmos., 113, 10.1029/2007jd009740, 2008.

960 Miller, J. B., Lehman, S. J., Montzka, S. A., Sweeney, C., Miller, B. R., Karion, A., Wolak, C., Dlugokencky, E.
961 J., Southon, J., Turnbull, J. C., and Tans, P. P.: Linking emissions of fossil fuel CO_2 and other anthropogenic trace
962 gases using atmospheric $^{14}CO_2$, J. Geophys. Res.-Atmos., 117, 1-23, 10.1029/2011jd017048, 2012.

963 Monni, S., Syri, S., and Savolainen, I.: Uncertainties in the Finnish greenhouse gas emission inventory, Environ.
964 Sci. Policy, 7, 87-98, https://doi.org/10.1016/j.envsci.2004.01.002, 2004.

965 Mues, A., Kuenen, J., Hendriks, C., Manders, A., Segers, A., Scholz, Y., Hueglin, C., Builtjes, P., and Schaap, M.:
966 Sensitivity of air pollution simulations with LOTOS-EUROS to the temporal distribution of anthropogenic
967 emissions, Atmos. Chem. Phys., 14, 939-955, 10.5194/acp-14-939-2014, 2014.

968 Nakicenovic, N., Alcamo, J., Davis, G., De Vries, B., Fenhann, J., Gaffin, S., Gregory, K., Grübler, A., Jung, T.
969 Y., Kram, T., La Rovere, E. L., Michaelis, L., Mori, S., Morita, T., Pepper, W., Pitcher, H., Price, L., Riahi, K.,
970 Roehrl, A., Rogner, H.-H., Sankovski, A., Schlesinger, M., Shukla, P., Smith, S., Swart, R., Van Rooijen, S.,
971 Victor, N., and Dadi, Z.: IPCC Special Report on Emissions Scenarios, Cambridge University Press, Cambridge,
972 UK, 2000.

973 Nassar, R., Napier-Linton, L., Gurney, K. R., Andres, R. J., Oda, T., Vogel, F. R., and Deng, F.: Improving the
974 temporal and spatial distribution of CO_2 emissions from global fossil fuel emission data sets, J. Geophys. Res.-
975 Atmos., 118, 917-933, 10.1029/2012jd018196, 2013.

976 Nathan, B., Lauvaux, T., Turnbull, J., and Gurney, K.: Investigations into the use of multi-species measurements
977 for source apportionment of the Indianapolis fossil fuel CO2 signal, Elementa, 6, 10.1525/elementa.131, 2018.

978 Nehrkorn, T., Eluszkiewicz, J., Wofsy, S. C., Lin, J. C., Gerbig, C., Longo, M., and Freitas, S.: Coupled weather
979 research and forecasting-stochastic time-inverted lagrangian transport (WRF-STILT) model, Meteorol. Atmos.
980 Phys., 107, 51-64, 10.1007/s00703-010-0068-x, 2010.

981 Netherlands PRTR: Netherlands Pollutant Release & Transfer Register: http://www.emissieregistratie.nl/, last
982 access: Mar 2018.

983 Palmer, P. I., O'Doherty, S., Allen, G., Bower, K., Bösch, H., Chipperfield, M. P., Connors, S., Dhomse, S., Feng,
984 L., Finch, D. P., Gallagher, M. W., Gloor, E., Gonzi, S., Harris, N. R. P., Helfter, C., Humpage, N., Kerridge, B.,
985 Knappett, D., Jones, R. L., Le Breton, M., Lunt, M. F., Manning, A. J., Matthiesen, S., Muller, J. B. A., Mullinger,
986 N., Nemitz, E., O'Shea, S., Parker, R. J., Percival, C. J., Pitt, J., Riddick, S. N., Rigby, M., Sembhi, H., Siddans,
987 R., Skelton, R. L., Smith, P., Sonderfeld, H., Stanley, K., Stavert, A. R., Wenger, A., White, E., Wilson, C., and
988 Young, D.: A measurement-based verification framework for UK greenhouse gas emissions: an overview of the
989 Greenhouse gAs Uk and Global Emissions (GAUGE) project, Atmos. Chem. Phys., 18, 11753-11777,
990 10.5194/acp-18-11753-2018, 2018.

991   Peters, W., Miller, J. B., Whitaker, J., Denning, A. S., Hirsch, A., Krol, M. C., Zupanski, D., Bruhwiler, L., and
992   Tans, P. P.: An ensemble data assimilation system to estimate CO_2 surface fluxes from atmospheric trace gas
993   observations, J. Geophys. Res.-Atmos., 110, 1-18, 10.1029/2005JD006157, 2005.
994   Peters, W., Krol, M. C., Van der Werf, G. R., Houweling, S., Jones, C. D., Hughes, J., Schaefer, K., Masarie, K.
995   A., Jacobson, A. R., Miller, J. B., Cho, C. H., Ramonet, M., Schmidt, M., Ciattaglia, L., Apadula, F., Heltai, D.,
996   Meinhardt, F., Di Sarra, A. G., Piacentino, S., Sferlazzo, D., Aalto, T., Hatakka, J., Ström, J., Haszpra, L., Meijer,
997   H. A. J., Van der Laan, S., Neubert, R. E. M., Jordan, A., Rodó, X., Morguí, J. A., Vermeulen, A. T., Popa, E.,
998   Rozanski, K., Zimnoch, M., Manning, A. C., Leuenberger, M., Uglietti, C., Dolman, A. J., Ciais, P., Heimann, M.,
999   and Tans, P.: Seven years of recent European net terrestrial carbon dioxide exchange constrained by atmospheric
1000   observations, Glob. Change Biol., 16, 1317-1337, 10.1111/j.1365-2486.2009.02078.x, 2010.
1001   Ramírez, A. R., De Keizer, C., and Van der Sluijs, J. P.: Monte Carlo analysis of uncertainties in the Netherlands
1002   Greenhouse Gas Emission Inventory for 1990 – 2004, Copernicus Institute for Sustainable Development and
1003   Innovation, Utrecht, 2006.
1004   Rao, P., Gurney, K. R., Patarasuk, R., Song, Y., Miller, C. E., Duren, R. M., and Eldering, A.: Spatio-temporal
1005   Variations in on-road CO2 Emissions in the Los Angeles Megacity, AIMS Geosciences, 3, 239-267,
1006   http://dx.doi.org/10.3934/geosci.2017.2.239, 2017.
1007   Raupach, M. R., Marland, G., Ciais, P., Le Quéré, C., Canadell, J. G., Klepper, G., and Field, C. B.: Global and
1008   regional drivers of accelerating CO_2 emissions, P. Natl. Acad. Sci. USA, 104, 10288-10293,
1009   10.1073/pnas.0700609104, 2007.
1010   Rayner, P. J., Raupach, M. R., Paget, M., Peylin, P., and Koffi, E.: A new global gridded data set of CO_2 emissions
1011   from fossil fuel combustion: Methodology and evaluation, J. Geophys. Res.-Atmos., 115, 10.1029/2009jd013439,
1012   2010.
1013   Sauter, F., Van Zanten, M., Van der Swaluw, E., Aben, J., De Leeuw, F., and Van Jaarsveld, H.: The OPS-model.
1014   Description of OPS 4.5.0, National Institute for Public Health and the Environment (RIVM) Bilthoven, 2016.
1015   Staufer, J., Broquet, G., Bréon, F. M., Puygrenier, V., Chevallier, F., Xueref-Rémy, I., Dieudonné, E., Lopez, M.,
1016   Schmidt, M., Ramonet, M., Perrussel, O., Lac, C., Wu, L., and Ciais, P.: The first 1-year-long estimate of the Paris
1017   region fossil fuel CO_2 emissions based on atmospheric inversion, Atmos. Chem. Phys., 16, 14703-14726,
1018   10.5194/acp-16-14703-2016, 2016.
1019   Su, H., Yang, Z. L., Niu, G. Y., and Wilson, C. R.: Parameter estimation in ensemble based snow data assimilation:
1020   A synthetic study, Adv. Water Resour., 34, 407-416, 10.1016/j.advwatres.2010.12.002, 2011.
1021   Super, I., Dellaert, S.N.C., Visschedijk, A.J.H., and Denier van der Gon, H.A.C.: Uncertainty analysis of a
1022   European high-resolution emision inventory of CO_2 and CO to support inverse modelling and network design,
1023   Atmos. Chem. Phys. Discuss., https://doi.org/10.5194/acp-2019-696, in review, 2019.
1024   Super, I., Denier van der Gon, H. A. C., Van der Molen, M. K., Sterk, H. A. M., Hensen, A., and Peters, W.: A
1025   multi-model approach to monitor emissions of CO_2 and CO from an urban–industrial complex, Atmos. Chem.
1026   Phys., 17, 13297-13316, 10.5194/acp-17-13297-2017, 2017a.
1027   Super, I., Denier van der Gon, H. A. C., Visschedijk, A. J. H., Moerman, M. M., Chen, H., Van der Molen, M. K.,
1028   and Peters, W.: Interpreting continuous in-situ observations of carbon dioxide and carbon monoxide in the urban
1029   port area of Rotterdam, Atmos. Pollut. Res., 8, 174–187, 10.1016/j.apr.2016.08.008, 2017b.

1030   Terrenoire, E., Bessagnet, B., Rouïl, L., Tognet, F., Pirovano, G., Létinois, L., Beauchamp, M., Colette, A., Thunis,

1031   P., Amann, M., and Menut, L.: High-resolution air quality simulation over Europe with the chemistry transport

1032   model CHIMERE, Geosci. Model Dev., 8, 21-42, 10.5194/gmd-8-21-2015, 2015.

1033   Tolk, L. F., Meesters, A. G. C. A., Dolman, A. J., and Peters, W.: Modelling representation errors of atmospheric

1034 CO_2 mixing ratios at a regional scale, Atmos. Chem. Phys., 8, 6587-6596, 10.5194/acp-8-6587-2008, 2008.

1035   Turnbull, J. C., Miller, J. B., Lehman, S. J., Tans, P. P., Sparks, R. J., and Southon, J.: Comparison of $^{14}CO_2$, CO,

1036   and SF_6 as tracers for recently added fossil fuel CO_2 in the atmosphere and implications for biological CO_2

1037   exchange, Geophys. Res. Lett., 33, 1-5, 10.1029/2005GL024213, 2006.

1038   Turnbull, J. C., Sweeney, C., Karion, A., Newberger, T., Lehman, S. J., Tans, P. P., Davis, K. J., Lauvaux, T.,

1039   Miles, N. L., Richardson, S. J., Cambaliza, M. O., Shepson, P. B., Gurney, K., Patarasuk, R., and Razlivanov, I.:

1040   Toward quantification and source sector identification of fossil fuel CO_2 emissions from an urban area: Results

1041   from the INFLUX experiment, J. Geophys. Res.-Atmos., 120, 292-312, 10.1002/2014jd022555, 2015.

1042   UNFCCC: Paris Agreement, UNFCCC, 2015.

1043   Van der Laan-Luijkx, I. T., Van der Velde, I. R., Van der Veen, E., Tsuruta, A., Stanislawska, K.,

1044   Babenhauserheide, A., Zhang, H. F., Liu, Y., He, W., Chen, H., Masarie, K. A., Krol, M. C., and Peters, W.: The

1045   CarbonTracker Data Assimilation Shell (CTDAS) v1.0: Implementation and global carbon balance 2001–2015,

1046   Geosci. Model Dev., 10, 2785-2800, 10.5194/gmd-10-2785-2017, 2017.

1047   Van der Laan, S., Van der Laan-Luijkx, I. T., Zimmermann, L., Conen, F., and Leuenberger, M.: Net CO_2 surface

1048   emissions at Bern, Switzerland inferred from ambient observations of CO_2, $\delta(O_2/N_2)$, and ^{222}Rn using a customized

1049   radon tracer inversion, J. Geophys. Res.-Atmos., 119, 1580-1591, 10.1002/2013JD020307, 2014.

1050   Van Jaarsveld, J. A.: The Operational Priority Substances model. Description and validation of OPS-Pro 4.1,

1051   National Institute for Public Health and the Environment, Bilthoven, 2004.

1052   Vogel, F. R., Thiruchittampalam, B., Theloke, J., Kretschmer, R., Gerbig, C., Hammer, S., and Levin, I.: Can we

1053   evaluate a fine-grained emission model using high-resolution atmospheric transport modelling and regional fossil

1054   fuel CO_2 observations?, Tellus B Chem. Phys. Meteorol., 65, 10.3402/tellusb.v65i0.18681, 2013.

1055   Wang, Y., Broquet, G., Ciais, P., Chevallier, F., Vogel, F., Wu, L., Yin, Y., Wang, R., and Tao, S.: Potential of

1056   European $^{14}CO2$ observation network to estimate the fossil fuel CO_2 emissions via atmospheric inversions, Atmos.

1057   Chem. Phys., 18, 4229-4250, 10.5194/acp-18-4229-2018, 2018.

1058   Whitaker, J. S., and Hamill, T. M.: Ensemble data assimilation without perturbed observations, Mon. Weather

1059   Rev., 130, 1913-1924, 10.1175/1520-0493(2002)130<1913:EDAWPO>2.0.CO;2, 2002.

1060   Zhou, Y., and Gurney, K. R.: Spatial relationships of sector-specific fossil fuel CO2 emissions in the United States,

1061   Global Biogeochem. Cycles, 25, 10.1029/2010gb003822, 2011.

1062

1063